

Feasibility and Performance Analysis of Neptune Aerocapture Using Heritage Blunt-Body Aeroshells

Athul Pradeepkumar Girija*, Sarag J. Saikia†, and James M. Longuski‡

Purdue University, West Lafayette, Indiana 47907

Shyam Bhaskaran§, Matthew S. Smith ¶, and James A. Cutts||

Jet Propulsion Laboratory, California Institute of Technology, Pasadena, California 91109

Large navigation and atmospheric uncertainties have historically driven the need for a mid-lift-to-drag (L/D) vehicle with $(L/D)_{\max}$ of 0.6–0.8 for aerocapture at Neptune. Most planetary entry vehicles flown to date are low- L/D blunt-body aeroshells with L/D less than 0.4. The lack of a heritage mid- L/D aeroshell presents a major hurdle for Neptune aerocapture, as the development a new entry vehicle incurs significant time and investment. Techniques which may allow Neptune aerocapture to be feasible using heritage low- L/D blunt-body aeroshells are investigated that obviate the need for mid- L/D aeroshells. A navigation study is performed to quantify the delivery errors, and a new guidance algorithm with onboard density estimation is developed to accommodate large atmospheric uncertainties. Monte Carlo simulation results indicate that the reduced navigation uncertainty and improved guidance scheme enable a blunt-body aeroshell with $L/D = 0.3\text{--}0.4$ to perform aerocapture at Neptune. The expected heat rate is within the capabilities of existing thermal protection system materials.

I. Introduction

Aerocapture is a maneuver in which a spacecraft uses aerodynamic drag to decelerate and perform orbit insertion. Neptune's great heliocentric distance and the need to achieve reasonable flight time lead to high arrival V_∞ and large orbit insertion ΔV . Propulsive insertion incurs significant mass penalty due to the large ΔV , where aerocapture is a promising alternative. Aerocapture at Neptune has been shown to substantially increase delivered mass and allow reduction in flight time compared to propulsive insertion [1–3]. Despite the potential benefits, aerocapture at Neptune presents significant challenges related to vehicle design and thermal protection system materials (TPS). The large navigation and atmospheric uncertainties drive the need for a vehicle with sufficient control authority to perform aerocapture without the spacecraft risking escape or undershooting the target capture orbit [4].

*Doctoral Candidate, School of Aeronautics and Astronautics; apradee@purdue.edu, AIAA Student Member.

†Research Assistant Professor, School of Aeronautics and Astronautics; ssaikia@purdue.edu. Currently CEO, Spacefaring Technologies Pvt Ltd.

‡Professor, School of Aeronautics and Astronautics; longuski@purdue.edu, AIAA Associate Fellow.

§Supervisor, Mission Design and Navigation Section; shyamkumar.bhaskaran@jpl.nasa.gov

¶Navigation Engineer, Mission Design and Navigation Section; matthew.s.smith@jpl.nasa.gov

||Program Manager, Solar System Exploration Directorate; james.a.cutts@jpl.nasa.gov

Several mission concepts and technology demonstration flights have proposed the use of aerocapture, but it has never been flown [5–9]. Hall et al. [10] showed that aerocapture could enhance missions to Venus, Mars, Titan, and Uranus and enable some missions to Jupiter, Saturn, and Neptune. Heritage low lift-to-drag ratio ($L/D \leq 0.4$) blunt body aeroshells and existing TPS materials are sufficient for aerocapture at Venus, Mars, and Titan [4, 11–14]. Aerocapture studies have historically used a mid lift-to-drag (L/D) vehicle with L/D of 0.6–0.8 to accommodate the large navigation and atmospheric uncertainties at Uranus and Neptune [15–19]. Aerocapture at Jupiter and Saturn is considered a long-term goal due to the extreme aerothermal conditions during the atmospheric pass. [4].

Until the early 2000s most aerocapture studies address feasibility at Earth and Mars, though some generic aerocapture studies evaluate its applicability at Uranus and Neptune [20, 21]. Detailed study of aerocapture at Neptune began only in the early 2000s due to a multi-center NASA effort funded by the In-Space Technology Program [11, 22–28]. The study concluded that aerocapture at Neptune is feasible using a vehicle with L/D of 0.6–0.8 and can deliver 1.4 times more mass to orbit compared to propulsive orbit insertion. In 2016, Spilker et al. [4] performed a study initiated by the NASA Planetary Science Division (PSD) to assess the readiness of aerocapture at all planetary destinations. The study concluded that aerocapture at Uranus and Neptune call for at least an additional study to assess the need for mid- L/D vehicles which require significant development and testing before use on planetary missions. The study recommends quantifying delivery errors at Neptune, investigation of improved flight control techniques, and other mission concept(s) such as pathfinder probes which may reduce the vehicle L/D requirement.

In 2016, Saikia et al. [19] performed an assessment of aerocapture at Uranus and Neptune in support of the NASA Ice Giants Pre-Decadal Survey Mission Study [29]. Saikia et al. demonstrated the importance of coupling between interplanetary arrival conditions and aerocapture feasibility at Uranus and Neptune. The study concluded that mid- L/D vehicles (L/D of 0.6–0.8) are required at Uranus and Neptune to accommodate the uncertainties, using uncertainty estimates available from Lockwood et al. [1]. Development and testing of a new mid- L/D vehicle requires substantial funding commitment and at least a decade's time. This merits investigation of approaches which obviate the need for mid- L/D vehicles. The study recommended several directions of future work: 1) investigate the feasibility of high-energy fast arrival interplanetary trajectories which allow for more control authority compared to conventional trajectories used for propulsive insertion architectures, 2) perform studies to better quantify the relevant uncertainties such as delivery errors from approach navigation and atmospheric uncertainties, and 3) investigate approaches such as guidance schemes with onboard density estimation, hybrid aerocapture-propulsive techniques, and a pathfinder entry probe. One or a combination of these techniques may allow the use of a heritage low- L/D vehicle for Neptune aerocapture thus obviating the need for a new mid- L/D vehicle, and leads to the objectives of the present study: 1) Assess the feasibility of Neptune aerocapture using heritage blunt-body aeroshells with L/D of 0.4 or less. 2) Provide statistical metrics of aerocapture vehicle performance using a representative interplanetary trajectory incorporating the state-of-the-art knowledge in navigation, atmospheric, and aerodynamic uncertainties.

In 2019, the NASA Outer Planets Analysis Group (OPAG) reiterated the potential and benefits offered by aerocapture for ice giant missions [30]. When combined with aerocapture, the Space Launch System (SLS) would enable trip times to Uranus and Neptune to be as short as 5 and 7 years respectively. Aerocapture offers substantial savings in flight time compared to a nominal 12 years to Uranus and more than 13 years to Neptune compared to propulsive insertion architectures. The Planetary Science Decadal Survey recommends a Uranus orbiter with probe as the third-highest priority Flagship-class mission in the next decade, after Mars Sample Return and Europa orbiter [31]. Between Uranus and Neptune, more difficult requirements of achieving orbit at Neptune appear to be the reason for Uranus being preferred over Neptune [31]. There is significant scientific interest in Neptune and Triton, as evident in the evaluation of mission concepts for both Uranus and Neptune in the NASA Ice Giants Pre-Decadal Mission Study [29] and the ESA Ice Giants Study [32]. Aerocapture strongly enhances and in some cases enable missions to either of the ice giants without being constrained by a substantial propulsive insertion mass penalty due to the large orbit insertion ΔV [2–4]. The present study aims to consolidate the state-of-the-art knowledge of aerocapture mission design to allow scientists, mission designers, and program managers to assess its readiness for a future ice giant mission.

II. Aerocapture Trade Space and Feasibility Analysis

Previous Neptune aerocapture studies have often been restricted to analysis of a single-point design with limited exploration of the underlying trade space. Multiple aerocapture studies have used a limited number of candidate interplanetary trajectories and vehicle designs to perform aerocapture systems analysis, and quantify the performance benefits compared to propulsive insertion [1, 10, 11, 13, 33]. The interplanetary trajectories are often optimized for propulsive insertion, and do not take into account the often differing requirements for aerocapture. In addition to the mass benefit, aerocapture can allow significantly shorter time of flights for outer solar system missions compared to propulsive insertion. Hughes [34] has compiled a catalog of short time of flight, high arrival V_∞ trajectories to Uranus and Neptune though their aerocapture feasibility aspects are yet to be investigated. Such high V_∞ trajectories greatly widen the interplanetary trajectory options for missions to Uranus and Neptune.

To accommodate for the large uncertainties at Uranus and Neptune the aerocapture vehicle must have sufficiently large L/D . All interplanetary entry missions flown to date have used ballistic or low- L/D vehicles ($L/D \leq 0.4$) and are considered high heritage entry systems. Studies investigating aerocapture at Neptune have used a mid- L/D vehicle (L/D of 0.6–0.8), assuming such a vehicle would be available. The non-availability of a mid- L/D vehicle presents a major hurdle for aerocapture at the ice giant planets. The present study introduces an approach to determine the required vehicle L/D considering a broad set of interplanetary trajectories and vehicle designs. In addition to the previously mentioned issues for aerocapture systems, constraints arising from launch vehicle performance, entry deceleration loads, aerodynamic heating are considered. The present work uses the “aerocapture feasibility chart” for rapid trade space exploration unifying interplanetary trajectory and vehicle design aspects of the problem.

Figure 1 shows the aerocapture feasibility chart for Neptune. The left chart shows the arrival V_∞ , time of flight, and launch C_3 for a comprehensive set of interplanetary trajectories from Earth to Neptune and shows the trade-off between these parameters for mission design. The trajectory data comes from two sources: the NASA Ice Giants Pre-Decadal Mission Study [29], and a set of high V_∞ trajectories made available to the authors by the Jet Propulsion Laboratory. The trajectories include both relatively slow arrival (defined by $V_\infty \leq 15$ km/s) trajectories used for propulsive insertion and fast arrival ($15 < V_\infty \leq 25$ km/s) trajectories which are feasible only with orbit insertion using aerocapture. To perform aerocapture the vehicle must enter the atmosphere within a narrow range of entry flight-path angles called the “theoretical corridor.” Entering too steep results in the vehicle undershooting the target apoapsis and possibly encountering aerodynamic heating beyond the TPS limits. Entering too shallow results in the vehicle not getting captured. The right chart in Fig. 1 shows contours of the theoretical corridor width (TCW), peak deceleration, peak stagnation-point heat rate \dot{q} , and total heat load as a function of the arrival V_∞ and vehicle L/D . A nominal deceleration limit of 30g is imposed. For the peak heat rate constraint, 8000 W/cm² is used based on Heatshield for Extreme Entry Environment Technology (HEEET) test results [35]; and a total heat load constraint of 600 kJ/cm² is used which is about twice the nominal stagnation point heat load for the Galileo entry probe [36].

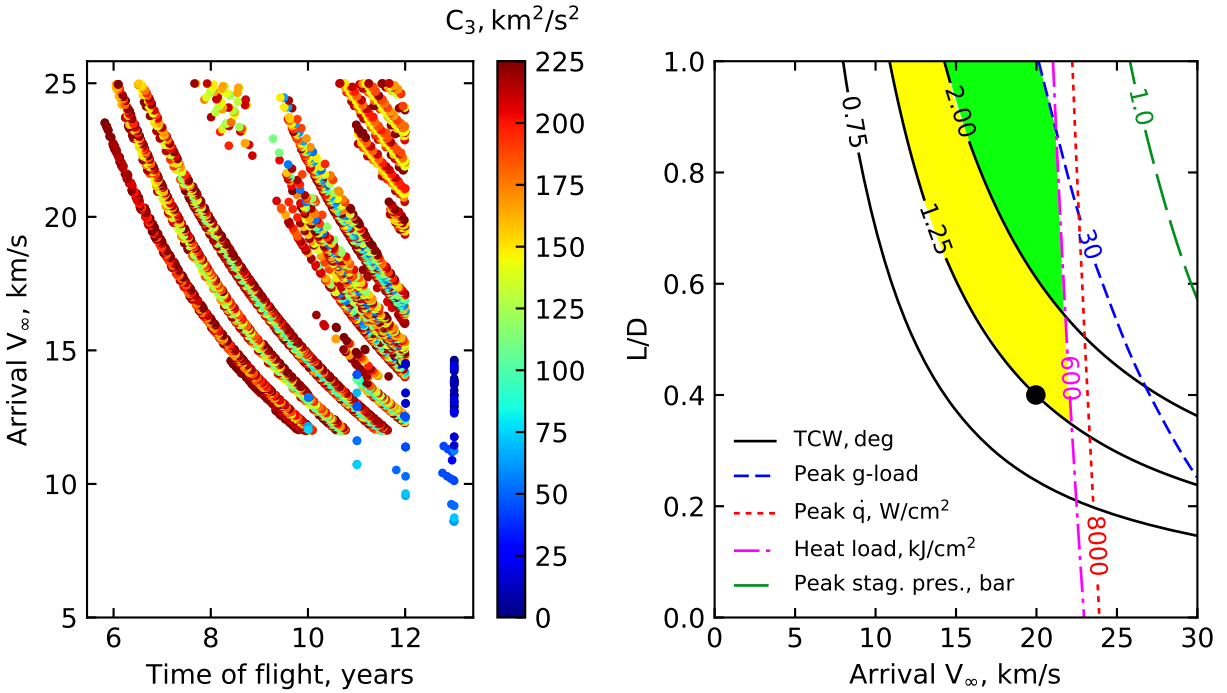


Fig. 1 Neptune aerocapture feasibility chart. The green region indicates the feasible design space for TCW requirement of 2.0 deg, for which the required L/D is 0.6–1.0 [1].

The green shaded area shows the feasible combinations of ($L/D, V_\infty$) for a TCW requirement of 2.0 deg [1], and deceleration and heating constraints bounding the feasible region. The bottom corner of the green shaded region

indicates the smallest L/D for which aerocapture is feasible if the required TCW = 2.0 deg. To minimize the required L/D , high arrival V_∞ trajectories are desired as the higher entry speed allows a larger theoretical corridor compared to slow arrival trajectories. The fast arrival trajectories using aerocapture also allow significantly shorter time of flight to Neptune (< 8 years) as compared to the conventional slow arrival trajectories using propulsive insertion (\approx 13 years). Figure 1 shows that propulsive insertion and aerocapture require a different class of interplanetary trajectories. Propulsive insertion requires arrival V_∞ to be small enough such that the propulsion system can handle the capture burn. Short time of flight trajectories typically have high arrival V_∞ , and results in large propellant mass requirement which in turn severely limits the useful delivered mass. On the other hand, aerocapture requires a high arrival V_∞ to minimize the L/D requirement. Interplanetary trajectories with arrival V_∞ less than a critical value (defined by vehicle L/D and the TCW requirement in Fig. 1) are infeasible for aerocapture. The range of feasible arrival V_∞ for aerocapture is bounded on the upper end by peak deceleration and TPS material and total heat load constraints.

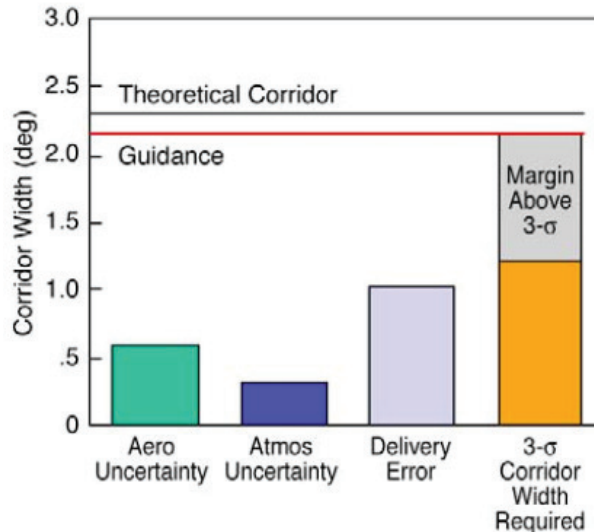


Fig. 2 Contribution of various uncertainties and root-sum-squared required corridor width for Neptune aerocapture as estimated by Lockwood et al. [1].

The TCW requirement is computed based on the navigation, atmospheric, and aerodynamic uncertainties to be accommodated by the aerocapture vehicle and it dictates the required L/D . The contributions of various uncertainties as quantified by Lockwood et al. [1] and the root-sum-squared required corridor width (RCW) are shown in Fig. 2. To ensure the aerocapture vehicle achieves the desired atmospheric exit conditions, the TCW should be greater than the estimated RCW with adequate safety margin. Failure to satisfy this criteria implies the vehicle risks crashing into the planet or not getting captured. Based on the estimated RCW in Fig. 2, a TCW of at least 2.0 deg is required and the required L/D falls in the range of 0.6–1.0 as seen in Fig. 1. If the uncertainties are reduced (for example by reducing

the delivery error) such that the TCW requirement is reduced to 1.25 deg, then the yellow shaded region in Fig. 1 becomes feasible in addition to the green region. The reduced TCW requirement lowers the L/D requirement. Figure 1 shows that if the TCW requirement is lowered to 1.25 deg, fast arrival trajectories with $V_\infty \geq 20$ km/s allow the vehicle L/D requirement to be lowered to 0.4. The selected baseline design ($L/D = 0.4$, $V_\infty = 20$ km/s) is indicated by the black circle. Further reduction in L/D is possible if the uncertainties are reduced even further, and TCW requirement is reduced to 0.75 deg, which may allow an Mars Science Laboratory (MSL) derived aeroshell with $L/D = 0.24$ to be used.

III. Aerocapture Mission Design

A reference interplanetary trajectory is selected to allow a future Cassini-style exploration of the Neptune system. A comprehensive set of trajectories considering a wide range of arrival V_∞ at Neptune is used to assess the broad interplanetary trajectory trade space. For the purpose of this study, a maximum allowable time of flight of 8 years is considered (compared to the 13-year baseline used in the Ice Giants Pre-Decadal Study [29]). The minimum delivered mass requirement is 2000 kg to Neptune orbit, and SLS Block 1B is the baseline launch vehicle. Based on the allowable time of flight, delivered mass requirement at Neptune, and the available launch vehicle performance, a set of feasible candidate trajectories is considered. The study assumes the use of an Apollo-like blunt-body aerocapture vehicle with a total mass of approximately 5000 kg; with an additional 1000 kg allotment for a cruise stage jettisoned before the maneuver. The study assumes that 40% of the arrival mass (i.e. before aerocapture, which includes aeroshell structure, TPS, etc.) is delivered to orbit [10]. This results in about 2000 kg delivered to Neptune orbit, comparable to the dry mass of Cassini spacecraft at Saturn. Trajectories with C_3 low enough to satisfy the delivered mass requirement and also meet the flight time constraint are selected. For the feasible set of interplanetary trajectories the minimum required vehicle L/D can be computed from the right chart in Fig. 1 based on their arrival V_∞ . If heritage blunt-body aeroshells are used, the L/D requirement must not exceed 0.4. The chart also demarcates constraints arising from deceleration loads, heat rate, and total heat load. Interplanetary trajectories that provide sufficient TCW, and do not violate the peak deceleration, and aerodynamic heating constraints are feasible options. From the set of feasible trajectories, one that maximizes delivered mass is a desired candidate. Alternatively, the mission designer may use a performance index based on a combination of time of flight and delivered mass.

Preliminary results indicate that a trajectory launching in February 2031, with a Jupiter flyby in June 2032, and arriving at Neptune in January 2039 is a promising candidate. The flight time is 7.87 years and the launch C_3 is 111 km^2/s^2 . The launch capability of SLS Block 1B with kick stage is 6250 kg at the desired C_3 [29]. Trajectories to Neptune with flight times less than 13 years are infeasible with propulsive insertion [29, 37]; and hence the use of aerocapture with SLS allows a 5 year reduction in flight time. The high energy trajectory with a fast arrival V_∞ of 20 km/s allows the use of a heritage blunt-body aeroshell with $L/D = 0.4$ if the Theoretical Corridor Width (TCW) requirement can be lowered to about 1.25 degrees as seen in Fig. 1. The expected peak heat rate is within the current

tested capability of HEEET TPS [35]. The study emphasizes that these are preliminary estimates using engineering correlations for the convective and radiative heating rates [38]. The selected reference trajectory is used for analysis of the approach navigation errors and aerocapture performance analysis.

Upon arrival near the Neptune sphere of influence, the spacecraft targets the aim point on the B-plane to achieve the desired entry flight-path angle (EFPA) at atmospheric interface and the target orbit inclination [39]. Radiometric and optical navigation is used to guide the spacecraft to achieve the desired trajectory. Trajectory correction maneuvers (TCMs) are performed to reduce targeting errors as the spacecraft approaches the Neptune system. On exit from the atmosphere after aerocapture, the spacecraft coasts to an apoapsis of 400,000 km and following a propulsive periapsis raise maneuver—establishes the science orbit of 4,000 km \times 400,000 km. The target apoapsis altitude is chosen to be close to Triton’s circular orbital radius. Two candidate inclinations for the science orbit to allow Triton flybys are: 1) 157 deg retrograde with respect to Neptune, and 2) 23 deg prograde with respect to Neptune which results in higher Triton encounter speeds compared to the prograde case. The retrograde entry results in higher planet-relative entry speeds and hence higher peak heat rate and heat load compared to the prograde entry.

Errors in the B-plane targeting translate to errors in EFPA at the atmospheric entry interface. Knowledge of the B-plane targeting uncertainty is critical to assessing aerocapture mission feasibility using low- L/D aeroshells. If the delivery error is beyond what the vehicle control authority can accommodate, the vehicle guidance control variable is saturated and the guidance algorithm is unable to achieve the desired capture orbit. Low- L/D blunt body aeroshells offer less control authority than mid- L/D aeroshells, and can only accommodate smaller EFPA uncertainties compared to mid- L/D aeroshells. Accurate estimation of the navigation uncertainties along with atmospheric and other uncertainties are key to determining if blunt-body aeroshells offer sufficient control authority for Neptune aerocapture.

Delivery navigation error from spacecraft approach at Neptune were last quantified in 2004 by Lockwood et al.[1], and is the dominant uncertainty component as seen in Fig. 2. Improvements in navigation techniques (higher performance camera, refined ephemerides etc.) could reduce the navigation uncertainty component and hence lower the vehicle L/D requirement. Atmospheric uncertainties at Neptune have been modeled in the Neptune Global Reference Atmospheric Model (Neptune-GRAM), but no improvements are available over the data used by Lockwood et al. [1]. Spilker et al. [4] recommends performing opportunistic stellar occultations of Uranus and Neptune to improve the atmospheric models, but also notes that the technique may only provide information at high altitudes and extrapolating to altitudes relevant to aerocapture carries greater uncertainties. A dedicated research effort using Voyager data combined with new ground-based observations and modeling efforts may reduce the atmospheric uncertainties at altitudes relevant to aerocapture. Aerodynamic uncertainties have been quantified for a mid- L/D vehicle at Neptune during the 2004 systems analysis study [1], but no estimates are available for a low- L/D vehicle. A refined estimate of the delivery error is presented, along with a discussion of the current state of atmospheric and aerodynamic uncertainties.

A. Selection of Target Capture Orbit

The target orbit size and inclination are important parameters for both aerocapture and the subsequent tour of the Neptune system. The present study assumes a target capture orbit in Triton's orbital plane with apoapsis altitude nearly equal to Triton's orbital radius (400,000 km) and periapsis altitude around 4,000 km. The basis of the assumption is that the ability to perform close targeted flybys of Triton will be a driver for a future Neptune mission. However, both larger and smaller capture orbits and other inclinations may be considered. For example, a highly elliptical orbit (apoapsis greater than about 1 million km) may be suitable for certain observations while close-in circular orbits may be ideal for magnetic field or gravity science. Because, highly elliptical orbits are prone to escape, the recommended option is to first aerocapture to a 400,000 km or lower apoapsis altitude orbit and then transfer to a higher orbit. Low circular orbits offer more corridor width and hence reduce the vehicle control requirement. However, low circular orbits also imply a short coast time to the first apoapsis where the periapsis raise maneuver must be performed. Previous studies using propulsive insertion have considered a retrograde target orbit to achieve low flyby speeds at Triton [29]. However, for aerocapture the retrograde entry heating rates are about five times greater compared to prograde entry as will be shown later in Sec. VIII. Hence from an aerothermal perspective a prograde capture orbit is favorable if the high flyby speeds does not compromise Triton science objectives. The mission designer must take into account all of the above trade-offs and their implications of the target orbit on aerocapture feasibility, performance, and overall mission cost and complexity.

IV. Uncertainty Quantification

The aerocapture vehicle should have sufficient control authority to compensate for delivery error from approach navigation, atmospheric density uncertainties, and aerodynamic uncertainties. Quantification of these uncertainties is essential to evaluate the required vehicle L/D and is discussed in more detail in the following subsections.

A. Navigation Uncertainty

For the reference interplanetary trajectory, standard navigation covariance analysis is used to quantify the entry flight-path angle uncertainty at atmospheric entry interface (defined at 1000 km above the 1 bar pressure level). In this process, tracking data measurements are simulated along the reference trajectory and input into a linearized least-squares filter to estimate the spacecraft orbit and other parameters; the filter also produces a covariance matrix containing the uncertainties of the estimated parameters. Details of the navigation covariance analysis process is beyond the scope of this paper; a description of the data, methodology, and current state-of-the-art is available in the study by D'Amario and Watkins [40]. A high level description and details relevant to the approach of Neptune are as follows.

For deep space missions, the tracking data includes Doppler and Range (which measures the line-of-sight velocity and distance of the spacecraft relative to a tracking station, respectively), and Delta Differential One-Way Ranging (Δ DOR), an interferometric data type in which the time delay of a radio signal from a spacecraft received at two tracking

stations is used to compute an angular location of the spacecraft in the plane-of-sky. In addition, images of natural bodies taken by an onboard optical navigation (OpNav) camera provides a target-relative data type, especially important for approaching bodies whose orbit is not well known, such as Triton. The observable for OpNav data is the center of the observed body in the camera field-of-view (FOV) relative to the inertial pointing direction of the camera, computed through various centroiding techniques [41]. Since this is fundamentally an angular measure, the higher the angular resolution of the camera, the higher the accuracy of the OpNav data. The angular resolution is specified in terms of the angle extended by a single camera pixel, the instantaneous field-of-view (IFOV). For this study, two candidate optical navigation cameras are considered: 1) a generic medium resolution camera (Mid-Res) with a relatively wide IFOV, and 2) a high resolution camera (Hi-Res) with physical characteristics similar to the Long Range Reconnaissance Imager Camera (LORRI) flown on the New Horizons spacecraft. The camera specifications are shown in Table 1. Table 2 lists the 1σ noise on all the data types assumed in the analysis, and the tracking schedule for the radio and OpNav data.

Table 1 Camera specifications

Camera	Specifications
Mid-Res	<ul style="list-style-type: none"> • IFOV: 60 μrad • FoV: 122 mrad • focal length: 500 mm
Hi-Res	<ul style="list-style-type: none"> • IFOV: 5 μrad • FOV: 5 mrad • focal length: 2,619 mm

Table 2 Data tracking schedules and assumed noise

Data type	Tracking schedule	1σ noise
Doppler	3×8 hrs/week	0.1 mm/s
Range	3×8 hrs/week	3m
Δ DOR	2 pairs/week	0.06 ns
OpNav	3 pictures/day (Triton OpNav begins at E-60 days)	1 pixel

The reference trajectory is obtained via numerical integration, with the force model including gravitational attraction from 8 planets, the Neptunian moons Triton and Nereid, and the spherical harmonic gravity terms J_2, J_4 for Neptune. Four impulsive burns are also modeled, at Entry (E) - 30, 7, 5, and 2 days, and finally, small impulsive burns every 3 days are also included to account for minor spacecraft attitude adjustments. The nominal value for all burns in the reference trajectory is 0, but they are included in the filter so that their error is included in the estimated covariance. Of special note is the Neptune ephemeris; since errors in Neptune's position at arrival is a major driver of the navigation

dispersion at entry, two cases were examined. The first case uses the current level of uncertainty in Neptune's orbit. The second case assumes the uncertainty in Neptune ephemeris could be reduced by a factor of 100. The latter is a hypothetical improvement based on assumptions of future Neptune observations*.

The integration of the reference trajectory, data simulation, and the estimation process is accomplished using the MONTE software set [42]. Typically, for deep space missions the estimated parameters include, in addition to the spacecraft state (position and velocity), dynamic parameters which affect the spacecraft orbit (such as ephemerides and gravity fields of nearby natural bodies), non-gravitational forces acting on the spacecraft (such as solar radiation pressure and thrusting events), and parameters which affect the data (such as range biases). Also, some parameters are included in the filter as so-called “considered” parameters. These are bias parameters which contribute to the overall error covariance but are not estimated by the filter. They are typically used to account for parameters which are difficult to model or are poorly observed but are included in the covariance to prevent overly optimistic uncertainties. Examples of these are media propagation effects on the radio signal, and motion of the Earth's crust which affect the location of the tracking stations. A complete list of standard filter parameters can be found in the article by D'Amario and Watkins [40]; for the analysis performed in this study, Table 3 lists all the relevant ones, along with their *a priori* 1σ uncertainty.

Table 3 Estimated navigation filter parameters and uncertainties

Parameter	<i>a priori</i> 1σ uncertainty
• Spacecraft state at epoch	5E4 x 5E4 x 5E4 (km, Cartesian)
	5E-1 x 5E-1 x 5E-1 (km/s, Cartesian)
• Neptune barycenter state	2328 x 790 x 434 (km, Cartesian)
	3.2E-6 x 4.2E-7 x 1.3E-7 (km/s, Cartesian)
• Triton state	5.8 x 11.6 x 8.4 (km, Cartesian)
	9.4E-5 x 6.8E-5 x 4.2E-5 (km/s, Cartesian)
• Nereid state	180 x 111 x 108 (km, Cartesian)
	1.6E-5 x 6.7E-6 x 1.2E-5 (km/s, Cartesian)
• Impulsive maneuvers (E-30, E-7, E-5, E-2)	5 cm/s per axis
• Small burns for repointing (every 3 days)	0.2 mm/s per axis
• Neptune pole	Right Ascension: 4.6E-2 deg Declination: 9.1E-3 deg
• Neptune barycenter GM	4.845 km ³ /s ²
• Neptune J ₂ , J ₄	1.5E-6, 9.6E-7
• Triton GM	6.3E-1 km ³ /s ²
• Stochastic range biases at stations	2 m

The standard coordinate frame for the integration and estimation is the International Celestial Reference Frame (ICRF), centered at Neptune, and the estimated state is provided in Cartesian coordinates at the beginning of the integration arc. For analyzing entry performance, however, the covariance estimate can be mapped forward in time

*William Folkner, Private communication

and rotated into more suitable coordinates. One of these is the B-plane, which is a plane centered at the target body (Neptune in this case), and perpendicular to the incoming asymptote of the trajectory [43]. The mapped covariance is projected onto the B-plane as an ellipse, with the uncertainties represented by the major and minor axis of the ellipse (SMAA, SMIA). The covariance can also be mapped to the EFPA, and the EFPA error is proportional to the magnitude of the B-vector in the B-plane.

The 1σ entry flight path angle uncertainty with current level of Neptune ephemeris is shown in Table 4. For the selected interplanetary trajectory with arrival $V_\infty = 20$ km/s, a vehicle with $L/D = 0.4$ entering prograde near the equator results in $\text{TCW} \approx 1.25$ deg. If the $\pm 3\sigma$ navigation uncertainty alone exceeds the TCW, atmospheric and aerodynamic uncertainties cannot be accommodated. Preliminary simulations indicated the 1σ delivery error cannot exceed 0.2 deg if a blunt body aeroshell with $L/D = 0.40$ is used for the reference interplanetary arrival conditions. Table 4 shows that radiometric tracking alone (i.e. without OpNav) cannot achieve the desired delivery accuracy. Optical navigation using a Mid-Res camera with specifications listed in Table 1, along with radiometric navigation is also unable to achieve the desired targeting accuracy. The Hi-Res camera significantly lowers the delivery error, and Data Cut Off (DCO) at E-07 meets the preliminary requirement and DCO at E-04 days exceeds it (indicated by the rows highlighted in green). The delivery error for the E-04 DCO with current ephemeris uncertainty is considered baseline for the remainder of the study. The EFPA errors for the scenario with 100x improvement in Neptune ephemeris were similar to that obtained with the current Neptune ephemeris for E-07 and E-04 DCO. The calculations with the improved ephemeris did not produce a significantly different result and hence are not reported.

Table 4 1σ EFPA uncertainty using current Neptune ephemeris

Only radiometric tracking, no OpNav			
DCO, days	B-plane ellipse SMAA \times SMIA, km	$1\sigma B $ error, km	1σ EFPA error, deg
E - 09	328.8×255.3	272.9	1.78
E - 07	327.5×254.2	271.3	1.77
E - 04	325.1×253.3	270.3	1.76
With radiometric tracking and OpNav (Mid-Res)			
E - 09	170.3×160.3	162.9	1.06
E - 07	151.5×144.1	146.3	0.95
E - 04	116.5×113.5	114.4	0.74
With radiometric tracking and OpNav (Hi-Res)			
E - 09	39.8×35.4	39.2	0.26
E - 07	30.5×26.9	30.1	0.20
E - 04	17.6×14.6	17.1	0.11

Results using current Neptune ephemeris and the Hi-Res camera is an improvement over the previous estimate in literature which was ± 0.17 deg (1σ) [1]. The smaller delivery error lowers the TCW requirement and hence the

required L/D as shown in Fig. 1. The results represent a preliminary assessment of the delivery uncertainties. Sources of error not considered in the study may inflate these uncertainties to some degree. The primary concern would be non-gravitational effects on the spacecraft from mis-modeled thrusting events, such as outgassing or momentum wheel desaturations. Other non-gravitational effects [44] that were not considered in the study include solar radiation pressure, but at Neptune distances, this should be a small effect. Finally, systematic errors in OpNav centerfinding of extended bodies, such as Triton, may also degrade the results. Future studies with improved spacecraft system definition can refine the estimation of delivery uncertainties.

B. Atmospheric Uncertainty

The large heliocentric distance presents a challenge to accurate measurement of Neptune's atmospheric characteristics. The Voyager 2 spacecraft remains the only spacecraft to provide a glimpse of the Neptune atmospheric profile during its flyby in 1989 [4, 45]. Despite the limited data and the uncertainties in measurements, Neptune-GRAM is the state-of-the-art atmospheric model for aerocapture trajectory analysis. GRAMs are engineering level models for planetary atmospheres, and are widely used for systems design and performance analysis of flight trajectories [1, 46, 47]. The atmosphere model implemented in Neptune-GRAM is based on the data from Voyager 2 radio science experiment, infrared interferometer-spectrometer (IRIS), and ultraviolet spectrometer (UVS) instrument [48]. Neptune-GRAM provides the density, temperature, pressure, winds and chemical composition as a function of altitude, latitude, longitude, season, and local time. The model accounts for: 1) uncertainty in analysis of Voyager data, 2) latitudinal variations in the atmospheric structure, and 3) temporal changes due to seasonal and diurnal variations [49].

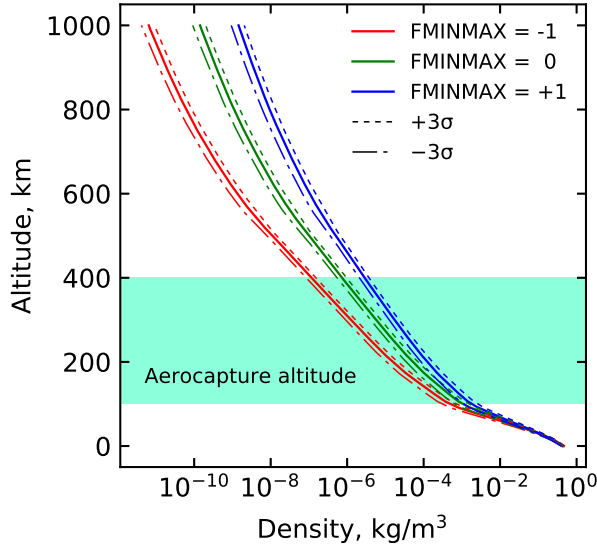


Fig. 3 Mean density profile variations from Neptune-GRAM by varying Fminmax from -1 to +1 and $\pm 3\sigma$ uncertainties about the mean profiles.

Neptune-GRAM uses a single input parameter “Fminmax” to account for uncertainty and variability of the mean density profile. $F_{\text{minmax}} = -1$ corresponds to the minimum mean density and $F_{\text{minmax}} = +1$ corresponds to the maximum mean density as shown in Fig. 3. Neptune-GRAM recommends using F_{minmax} near 0 for near-equatorial entry at equinox, negative F_{minmax} for polar entry during winter, and positive F_{minmax} for polar entry during the summer. Neptune-GRAM also provides the expected $\pm 3\sigma$ variation of the mean profile about the selected F_{minmax} value as shown in Fig. 3. The full range of F_{minmax} along with the 3σ dispersion is expected to cover the worst-case uncertainty in mean density profile. For aerocapture at Neptune, knowledge of the density profile uncertainty is most important in the altitude range 100 km to 400 km which is referred to as the aerocapture altitude range. Aerodynamic forces are negligible above 400 km and the minimum altitude during the aerocapture maneuver is well above 100 km for a wide range of vehicle L/D and arrival V_∞ . Neptune-GRAM also provides high frequency density perturbations superimposed on the mean profiles to account for random variations expected in the atmosphere as seen in Fig. 4. The parameter “rpscale” controls the high frequency variability of the atmospheric density and ranges from 0 to 2, with 0 indicating no perturbations and 2 indicating the highest perturbation amplitude. Previous studies used a nominal value of $rpscale = 1.0$, and lower values such as 0.5 indicate lower high frequency content. Previous studies have recommended using a smaller range of F_{minmax} depending on the arrival season and entry latitude instead of the full range. Lockwood et al. [1] used $0.60 \leq F_{\text{minmax}} \leq 0.93$ for an aerocapture vehicle flying in low latitudes in the season corresponding to the arrival time. The present study uses the full range of F_{minmax} from -1 to +1 as a worst-case estimate of the atmospheric uncertainties.

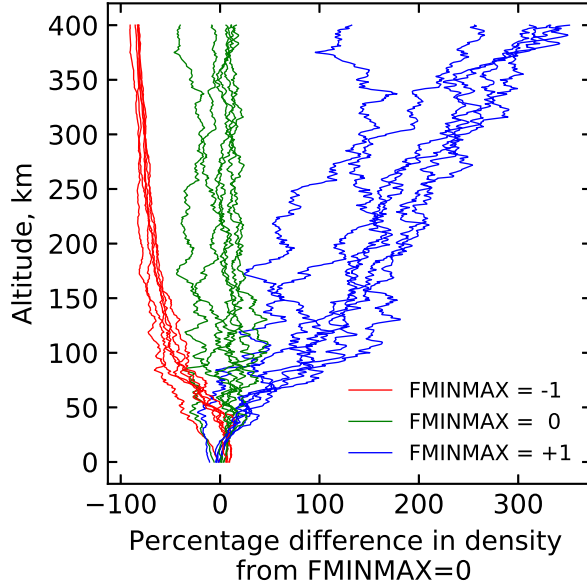


Fig. 4 Random perturbed density profiles from Neptune-GRAM for different values of F_{minmax} [1].

Better knowledge of the atmosphere from ground based observations and modeling may reduce the atmospheric

variability both in terms of mean profile and high frequency content. It is possible that existing observations when combined with global circulation models could constrain the range of Fminmax depending on the arrival season, and is worth further investigation. The present study investigates a novel approach called a pathfinder probe recommended by Spilker et al [4]. An entry probe enters the atmosphere several weeks ahead of the main aerocapture vehicle and relays the in-situ atmospheric density data. The aerocapture vehicle performs a trajectory correction maneuver to adjust the target entry flight-path angle, and is discussed in further detail in Section VII.

C. Aerodynamics Uncertainty

The vehicle aerodynamic control authority for bank angle modulation is quantified by the hypersonic trim lift-to-drag ratio $(L/D)_{\text{trim}}$ at the nominal trim angle of attack. Uncertainties in the mass distribution, ablation of the TPS material during aerocapture, shape changes, and mass imbalances translate into uncertainty in the vehicle $(L/D)_{\text{trim}}$. Quantification of aerodynamics uncertainties is important for entry vehicle performance analysis [50, 51], but is outside the scope of the present work. The present study uses a 10% 3σ dispersion about the nominal $(L/D)_{\text{trim}}$ as a representative estimate based on MSL entry vehicle aerodynamics reconstruction data [52]. Entry at Neptune presents a different and significantly more severe aerothermal environment than at Mars or Titan due to the higher entry speed and the H₂-He atmosphere. Additional study is required to quantify the aerodynamics uncertainties for a Neptune aerocapture vehicle using CFD and other numerical methods for prediction of TPS ablation during the maneuver.

V. Guidance Scheme

The aerocapture guidance algorithm guides the vehicle from the entry interface through atmospheric flight such that a desired set of terminal conditions are achieved when the vehicle exits the atmosphere. The desired terminal conditions at atmospheric exit allows the spacecraft to achieve the target capture orbit apoapsis and inclination. The present work uses bank angle modulation as the control method. Bank angle modulation uses an aeroshell which provides lift from offsetting the center of gravity with respect to the symmetry axis. The lift vector is rotated around the velocity vector by banking the vehicle and the bank angle is the sole control variable. Bank angle modulation has been successfully used on entry vehicles such as Apollo and the Mars Science Laboratory (MSL) and is considered a high-heritage flight control technique for low- L/D blunt body aeroshells [53, 54]. The guidance scheme used in the present work is a derivative of the Analytical Predictor-Corrector developed by Cerimele and Gamble [55]. The guidance consists of two phases: 1) the equilibrium glide phase, and 2) the exit phase as shown in Fig. 5. In the equilibrium glide phase, the vehicle attempts to maintain equilibrium glide condition i.e. altitude acceleration $\ddot{h} = 0$. The bank angle command δ_{CMD} during the equilibrium glide phase is computed as [55]

$$\cos \delta_{\text{CMD}} = \cos \delta_{\text{eq. gl.}} - G_{\dot{h}} \dot{h} + G_{\bar{q}} \left(\frac{\bar{q} - \bar{q}_{\text{ref}}}{\bar{q}} \right) \quad (1)$$

where $\cos \delta_{\text{eq. gl.}}$ is the calculated equilibrium glide bank angle to which increments are added, and is given by [55]

$$\cos \delta_{\text{eq. gl.}} = \frac{mg}{C_L \bar{q} S} \left(1 - \frac{v^2}{gr} \right) \quad (2)$$

where, m is the vehicle mass, g is the local gravitational acceleration, C_L is the vehicle lift coefficient, \bar{q} is the dynamic pressure, S is the aerodynamic reference area, v is the atmosphere relative speed, and r is the radial distance from the center of the planet. G_h and $G_{\bar{q}}$ refer to the gain parameters and are chosen based on the method developed by Cerimele and Gamble [55] described in Appendix A. The reference dynamic pressure \bar{q}_{ref} is computed as [55]

$$\bar{q}_{\text{ref}} = -\frac{mg}{0.75 C_L S} \left(1 - \frac{v^2}{gr} \right) \quad (3)$$

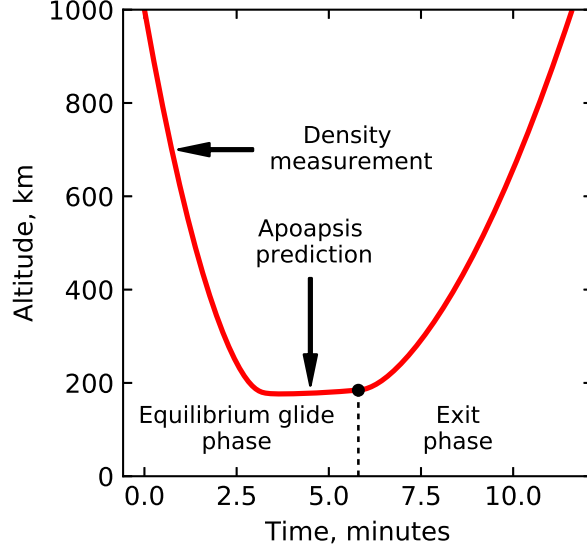


Fig. 5 Altitude history of the aerocapture maneuver showing the equilibrium glide phase and exit phase of the guidance algorithm.

A key feature of the guidance algorithm proposed in the present work is the onboard density estimation during the descending leg of the aerocapture maneuver. The vehicle uses the accelerometer measurements to estimate the atmospheric density during the equilibrium glide phase until a predetermined altitude rate \dot{h} is exceeded.

$$\rho_{\text{est}} = \frac{2ma_{\text{drag}}}{SC_D v^2} \quad (4)$$

where, ρ_{est} is the estimated density, a_{drag} is the measured drag acceleration, and C_D is the drag coefficient. The present study assumes the drag deceleration can be accurately estimated from onboard accelerometer readings [56, 57]. Figure 6 shows the comparison of actual and estimated density profiles for a vehicle with $L/D = 0.4$ entering Neptune retrograde

equatorial at 33 km/s (planet-relative speed) and accelerometer measurement frequency of 2 Hz. For altitudes below the minimum altitude at which density measurements are available, the algorithm extrapolates the density using an exponential model. The extrapolation uses the density estimate and computed scale height at the minimum altitude at which a measurement is available. The blue circle in Fig. 6 indicates the minimum altitude at which measurement was available, beyond which the profile is extrapolated. Figure 7 shows the percentage error in density estimation as a function of altitude. Potential sources of error in the density measurement such as data noise, uncertainty in vehicle mass and speed are not considered in the present study. The effect of turbulent buffeting, data noise and filtering, sensor response time, and computational cost of constructing a reliable density function using onboard computing resources are beyond the scope of the present work.

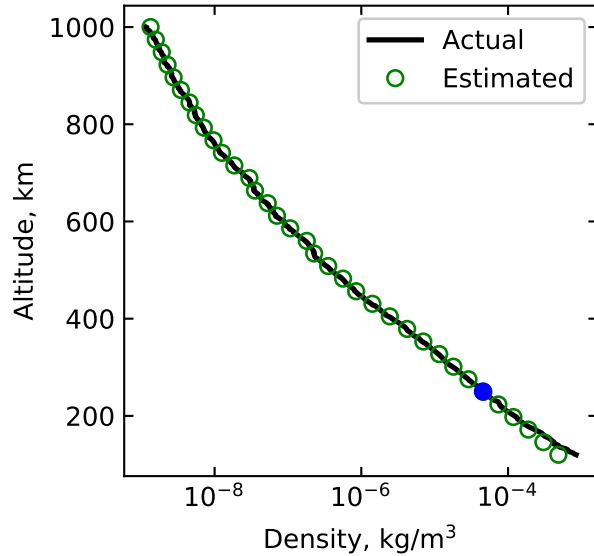


Fig. 6 Comparison of an actual perturbed random profile from Neptune-GRAM and estimated density profile from measured drag deceleration.

While onboard density estimation is proposed by many studies addressing aerocapture at Mars [57–59], its application to Neptune aerocapture has not been studied. Onboard density estimation significantly improves the guidance performance compared to using a preset density profile, and is of critical importance to aerocapture at Neptune due to low theoretical corridor width compared to Mars or Titan. Encountering a higher than expected density atmosphere could result in failure due to undershooting of the target apoapsis; a less dense atmosphere can result in apoapsis overshoot. Worst case scenarios involving low density atmosphere can result in the spacecraft leaving the atmosphere without getting captured. The proposed guidance scheme is shown to be able to achieve satisfactory performance even with large atmospheric uncertainties as shown in Section VIII.

Once a predetermined altitude rate \dot{h} threshold is exceeded, the vehicle starts predicting its apoapsis altitude at exit using full lift up for the remainder of the atmospheric flight. The prediction is done by numerically integrating the

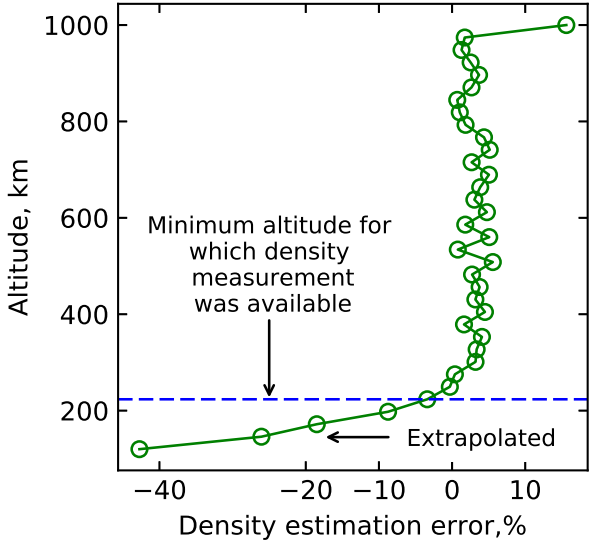


Fig. 7 Density estimation error. Below the minimum altitude for which on-board measurements are available, an exponential extrapolation is used.

equations of motion using the density profile measured during the descending leg of the aerocapture maneuver as shown in Fig. 5. When the predicted apoapsis altitude at exit is sufficiently close to the desired value, the exit phase is initiated and the vehicle pulls out of the atmosphere with full lift up for the remainder of the atmospheric flight. Density pockets and density shears are not modeled in Neptune-GRAM and may be a concern for aerocapture vehicles [60]. A case for concern would be if the density pockets are localized, and not encountered by the vehicle during the descending leg but only during the ascending leg resulting in erroneous apoapsis prediction. Further study is required to investigate the magnitude and spatial extent of density pockets in ice giant atmospheres and its effect of aerocapture performance.

The bank angle commanded to target the desired apoapsis will result in an out-of-plane force component for bank angles other than 0 deg (lift up) or 180 deg (lift down). The out-of-plane force component will cause the inclination to change as the vehicle flies through the atmosphere. Since bank angle is the only control available to target both the apoapsis at exit and the inclination, the strategy adopted is to perform bank angle reversals when the inclination exceeds prescribed bounds [55]. Because the maximum roll rate is limited, the vehicle will take a few seconds to complete the roll reversal and lead to some error in apoapsis targeting. The present study focuses only on the apoapsis targeting and leaves the inclination unconstrained for simplicity. Inclination errors from the atmospheric pass are expected to be small and can be corrected along with the periapsis raise maneuver. Additional study is required to include inclination targeting in the proposed guidance scheme, and analyze its effect on apoapsis targeting accuracy.

VI. Hybrid Propulsive-Aerocapture Concept

The hybrid propulsive-aerocapture concept refers to a technique where rocket propulsion provides a component of the deterministic ΔV for orbit insertion along with aerocapture. Using a combination of aerocapture and propulsion has been suggested as a method to reduce the vehicle L/D requirement for ice giant missions by Spilker et al. [4]. The present work considers two hybrid approaches which showed the potential to enable use of low- L/D blunt body aeroshells at Neptune.

The first approach involves aerocapture into an initial orbit with apoapsis lower than the planned science orbit, and then propulsively boosting the apoapsis to the desired orbit. The small initial capture orbit widens the theoretical corridor (TCW) and hence lowers the required vehicle L/D . An additional advantage of a small initial orbit is that it reduces the risk of accidental escape following aerocapture. The primary performance penalty for this hybrid approach is the propulsive ΔV cost for the apoapsis raise maneuver, as a high propulsive ΔV implies significant mass penalty. Additional risks from a small capture orbit include: 1) increased ring plane crossing hazard (particularly if the initial apoapsis is close to or inside the rings) and 2) less available time for orbit determination and corrective maneuvers compared to large orbits which have a several day coast period to the first apoapsis. Figure 8 shows the effect of initial capture orbit period on vehicle L/D requirement. The TCW constraint lines show the 2.0 deg contours for a range of initial capture orbits. The analysis assumes the desired science orbit has a 20-day period with periapsis radius of 1.1 Neptune radius. The green shaded patch shows the feasible set of $(L/D, V_\infty)$ if the initial capture orbit is 20 days. If a smaller one-day capture orbit is used, the blue patch becomes feasible, lowering the L/D requirement. After the periapsis raise maneuver, an apoapsis raise maneuver is performed at the periapsis.

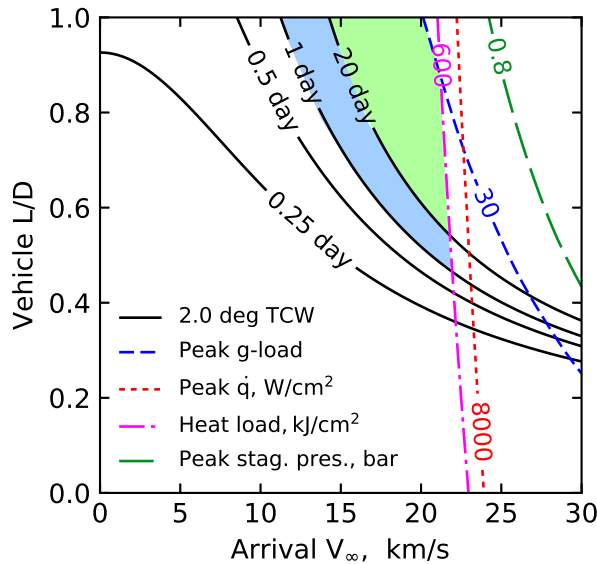


Fig. 8 Effect of initial capture orbit period on vehicle L/D requirement. Shaded regions show the feasible set of $(L/D, V_\infty)$ for 20 day and 1 day capture orbits.

Table 5 Minimum required L/D and deterministic propulsive ΔV cost for hybrid aerocapture-propulsive approach using small initial capture orbits, $V_\infty = 20$ km/s, target science orbit period = 20 days

Initial capture orbit period, days	Initial apoapsis altitude, km	$(L/D)_{\min}$	Apoapsis raise ΔV , m/s
20	1,553,575	0.61	0
1	166,163	0.51	1,252
0.5	85,543	0.45	2,148
0.25	34,755	0.38	3,658

Table 5 shows the minimum required L/D using different capture orbits for arrival at $V_\infty = 20$ km/s, and the apoapsis raise ΔV cost to achieve the 20-day science orbit. Using a small capture orbits does lower the L/D requirement (but not significantly to enable use of low- L/D aeroshells with reasonable ΔV penalty). Capture orbits less than one-day incur prohibitively high apoapsis raise ΔV and ring plane crossing hazard due to the low initial apoapsis. ΔV of 2 km/s or greater begin to approach the value for purely propulsive insertion, and accommodation of large propellant tanks inside an aeroshell presents another challenge.

The second hybrid approach involves aerocapture followed by a propulsive ΔV maneuver immediately after atmospheric exit as shown in Fig. 9. The propulsive ΔV capability allows a wider of range of entry flight path angles than conventional aerocapture and hence increases the TCW. $TCW_{\Delta V}$ indicates the modified theoretical corridor width with the additional ΔV , and is equal to the TCW for conventional aerocapture when $\Delta V = 0$. The ΔV corrects for the deficit in speed for a steeper entry than aerocapture, and corrects for excess speed in the case of a shallower entry than possible with aerocapture alone. The propulsive ΔV thus augments control authority and may allow reduction in vehicle L/D requirement. As with the first approach, the primary penalty for this approach is the propellant mass associated with the ΔV maneuver. In addition, the spacecraft has to autonomously determine its orbital state, compute the correction maneuvers, and execute the propulsive burn without any ground intervention immediately after atmospheric exit.

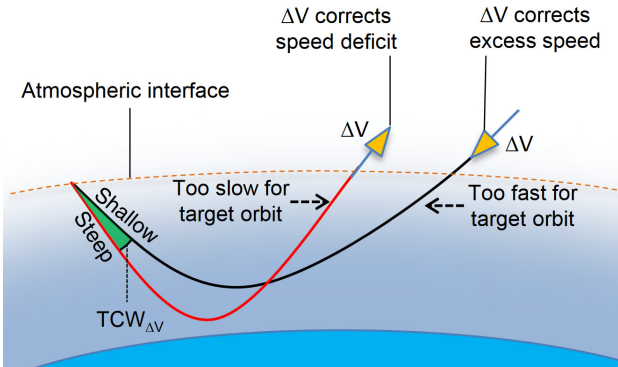


Fig. 9 Second approach where a propulsive ΔV at atmospheric exit augments control authority.

Figure 10 shows the effect of additional propulsive ΔV on the required vehicle L/D . The TCW constraint lines

show the 2.0 deg contours for a range of allowable propulsive ΔV . The green shaded area shows the feasible set of $(L/D, V_\infty)$ for conventional aerocapture with no ΔV maneuver at exit. If a propulsive ΔV maneuver of 1 km/s is allowed, the blue patch becomes feasible in addition to the green area, lowering the L/D requirement. After the ΔV maneuver is performed the vehicle has the correct speed to coast to the target apoapsis and following a periapsis raise maneuver enters the desired science orbit.

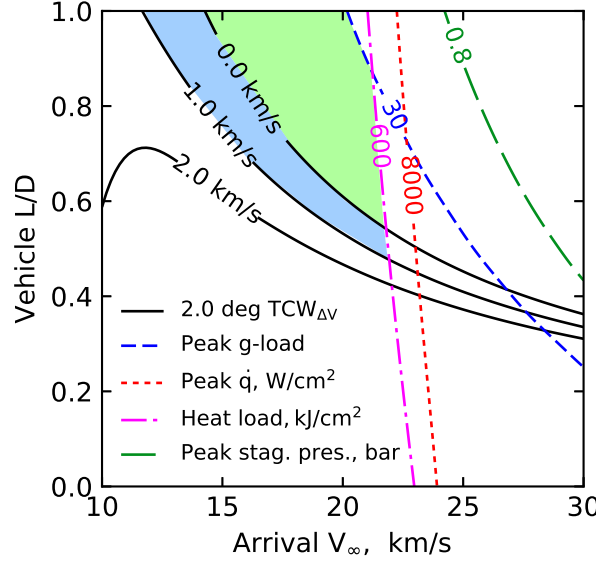


Fig. 10 Feasibility chart showing the effect of allowable propulsive ΔV at exit on vehicle L/D requirement.

Table 6 shows that the additional propulsive ΔV capability widens the theoretical corridor and thus lowers the L/D requirement. However, the reduction in required L/D is small and is not sufficient to enable the use of low- L/D aeroshells within a reasonable ΔV of 1 km/s. The propulsive ΔV required to allow use of heritage aeroshells is prohibitively high and leads to unacceptable propellant mass penalty for this hybrid propulsive-aerocapture concept. The propellant mass penalties outweighs the performance benefits and likely introduces additional cost and complexity.

Table 6 Minimum required L/D for hybrid propulsive-aerocapture approach with a propulsive ΔV maneuver at atmospheric exit, $V_\infty = 20$ km/s, target science orbit period = 20 days

Allowable propulsive ΔV , km/s	$(L/D)_{\min.}$
0.0	0.61
0.5	0.58
1.0	0.54
1.5	0.51
2.0	0.47

VII. Pathfinder Probe Concept

The present study investigated the option of sending a pathfinder entry probe into Neptune's atmosphere several weeks ahead of the main aerocapture vehicle reaching the atmospheric entry interface. The objective of the pathfinder probe is to measure the in-situ atmospheric profile and thus reduce the uncertainty in atmospheric profile prior to the aerocapture vehicle arriving at Neptune. Before the discussion of the pathfinder probe concept, it is insightful to discuss the “targeting problem” for aerocapture to illustrate the combined effect of navigation and atmospheric uncertainties. The targeting problem refers to the selection of a nominal target entry flight-path angle (EFPA) for the aerocapture maneuver. Several weeks ahead of entering Neptune, the approach navigation maneuvers target the aim point on the B-plane to allow the spacecraft to reach the atmospheric interface at the selected nominal EFPA.

The TCW is bounded by the shallowest and steepest acceptable EFPA for aerocapture. Figure 11 shows the TCW for a vehicle with $L/D = 0.4$ entering Neptune's atmosphere retrograde at the equator at a planet-relative speed of 33 km/s for $F_{\text{minmax}} = -1, 0, \text{ and } +1$. These values of F_{minmax} correspond to the minimum, average, and maximum mean density profiles from Neptune-GRAM. Theoretically, if the vehicle enters at any EFPA within the TCW the guidance algorithm can command the appropriate bank angle profile to achieve the desired exit conditions. However, simulations indicate that entry near the shallow limit of the corridor which requires almost full lift down for the entire trajectory are very sensitive to density perturbations. Such full lift down trajectories are not flyable in practice due to the risk of flyaway without getting captured. The hatched regions in Fig. 11 show the portion of the corridor rendered inaccessible due to the sensitivity of trajectories near the shallow limit using the guidance algorithm described in Section V and parameters listed in Appendix A. Thus the usable corridor for Neptune aerocapture is smaller than the theoretical corridor. Though the width of the corridor is not very sensitive to F_{minmax} , the shallow and steep bounds of the usable corridor change significantly based on the mean density profile and leads to the targeting problem. The selected nominal EFPA should be such that the $\pm 3\sigma$ navigation uncertainty falls within the usable corridor for the entire range of mean density profile uncertainties. Targeting the selected nominal EFPA allows the aerocapture vehicle to achieve the desired exit conditions for any mean atmospheric profile within the specified uncertainty.

In the present study, it is seen that a 3σ EFPA uncertainty of 0.33 deg (see Table 4) shown in Fig. 11 is not small enough to accommodate the entire range of mean density profiles from $F_{\text{minmax}} = -1$ to $+1$. There is no target EFPA that would allow both the $+3\sigma$ and -3σ delivery error to fall within the usable corridor for the range of atmospheric uncertainties considered. If the vehicle encounters the lowest density atmosphere (i.e. $F_{\text{minmax}} = -1$), and the EFPA falls outside $+3\sigma$, then the vehicle risks not getting captured. To minimize the risk of escape, the target EFPA is chosen such that the $+3\sigma$ delivery error falls just within the usable corridor for the minimum density atmosphere. For the case with the maximum density atmosphere (i.e. $F_{\text{minmax}} = +1$), the target EFPA itself and the -3σ delivery error fall below the theoretical corridor, which implies that the vehicle will undershoot the apoapsis altitude in such a scenario.

Simulations indicate that off-nominal EFPA outside $+3\sigma$ are very likely to flyaway without getting captured, while

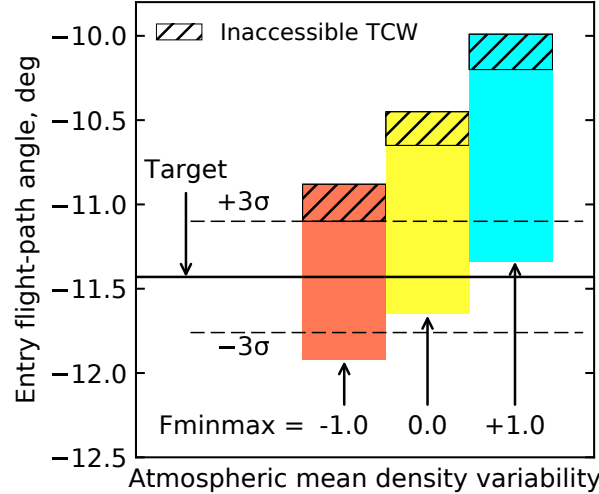


Fig. 11 The colored blocks show the theoretical corridor for various mean density atmospheric profiles. The target EFPA is chosen to minimize the risk of escape.

off-nominal EFPA outside -3σ will only likely result in undershoot of apoapsis but certainly not crash into the planet. The flyway case will almost certainly lead to loss of mission, while the apoapsis undershoot can be corrected using propulsive maneuvers and Triton gravity assists during the course of the mission. It is recommended to bias the target EFPA towards the steep side of the usable corridor to provide sufficient safety margin against the flyaway scenario for minimum density atmosphere, even if the -3σ EFPA bound falls outside the usable corridor for the maximum density atmosphere. Two possible options to increase the safety margin are: 1) decrease the navigation uncertainties further, and 2) reduce the atmospheric uncertainties. The pathfinder probe concept aims to use the second option of reducing atmospheric uncertainties to improve the safety margin against accidental escape.

The concept of operations for the pathfinder probe is as follows. Ahead of the main aerocapture vehicle reaching Neptune, an atmospheric entry probe is released from the main spacecraft. The carrier spacecraft also releases one or more SmallSats on a flyby trajectory with their arrival timed so as to act as a data relay from the probe during entry. The probe coasts to Neptune, while the main spacecraft performs a small propulsive burn such that it arrives at entry interface for aerocapture a few weeks after the probe entry. The probe measures the density in-situ (from accelerometer measurements), along with atmospheric structure and composition. The data is relayed to the main spacecraft via the SmallSats, which in turn relay the data back to Earth. The present study hypothesizes that the in-situ data when coupled with improved atmospheric models and ground based observation campaigns can reduce the uncertainty in the mean density profile to be encountered by the main aerocapture vehicle. The aerocapture vehicle then performs a small TCM to target the optimal EFPA based on the improved atmospheric profile knowledge.

Quantification of the atmospheric uncertainty reduction from a pathfinder entry probe is not possible at the level of the study. For illustration, the present study assumes that the pathfinder probe data is able to constrain the atmospheric

uncertainties such that $0.6 \leq F_{\min\max} \leq 0.8$ instead of the full range of $F_{\min\max}$ from -1 to +1. With the reduced uncertainty in $F_{\min\max}$, the target EFPA can be chosen so as to provide sufficient margin against escape above 3σ in the case of low density atmosphere, and against undershoot in the case of high density atmosphere as shown in Fig. 12. The pathfinder probe allows optimal selection of the target EFPA to minimize the risk of accidental escape or apoapsis undershoot. The pathfinder probe can improve the safety margin for aerocapture against escape and undershoot scenarios. Constraints on the timing of probe and SmallSat release, data transmission from the probe, propulsive ΔV for deflection maneuvers, the time available for data analysis and command upload to spacecraft for targeting the optimal EFPA are recommended for further study. It may be possible to let the relay SmallSat carry the pathfinder probe, and the SmallSat separate several months ahead of the main spacecraft reaching Neptune to keep the deflection maneuver ΔV reasonably low. If the two spacecraft can separate before the Jupiter gravity assist, it may be possible to further reduce the required deflection ΔV to achieve the few weeks separation between the pathfinder probe and the main spacecraft reaching Neptune; though this will add significant complexity to the mission architecture and spacecraft systems.

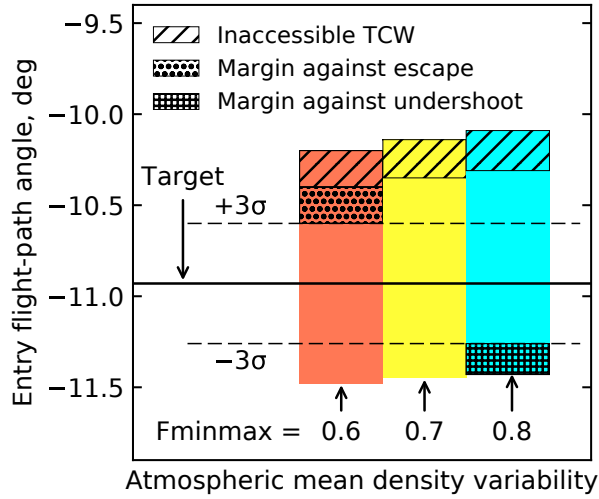


Fig. 12 Reduced atmospheric uncertainty from a pathfinder probe allows target EFPA selection such that both $+3\sigma$ and -3σ delivery errors fall within the usable corridor.

Inclusion of a pathfinder probe (in addition to a main entry probe) will add cost and complexity to the mission architecture. The design of the pathfinder probe is not part of the study, and assumes that the primary mission can accommodate the additional mass. The possibility of the pathfinder probe failing to accomplish its mission should be considered, due to entry probe failure, loss of data etc. Loss of the pathfinder probe cannot be a single point failure for the main aerocapture vehicle and should be capable of performing the maneuver with sufficient safety margin even if the data from the pathfinder probe is lost.

In the following section on performance analysis, the hybrid aerocapture approaches in Sec.VI are not considered further. The improved navigation uncertainty estimates from Sec. IV, the guidance scheme with onboard density

estimation from Sec.V, and the use of a pathfinder probe from Sec.VII are considered for aerocapture performance analysis using a blunt-body aeroshell.

VIII. Performance Analysis

Monte Carlo analysis is used to quantify the vehicle performance in the presence of combined navigation, atmospheric, and aerodynamic uncertainties. Nominal values of the parameters used and the associated uncertainties are listed in Table 7. The target entry flight-path angle is chosen based on the discussion presented in Section VII. For arrival $V_\infty = 20$ km/s of the reference interplanetary trajectory, the planet/atmosphere relative entry speed can range from 28 km/s for prograde entry to 33 km/s for retrograde entry. The location and width of the entry corridor changes as a function of the planet-relative entry speed and must be accounted for in aerocapture guidance analysis. The arrival declination is 8.8 deg, the entry latitude and heading angles can be computed based on the target orbit inclination [39]. The heading angle is defined as the angle between the velocity vector and the local parallel of latitude following the definition by Vinh et al. [61]. To simplify the trajectory analysis, the aerocapture simulations in this study use equatorial retrograde (180 deg heading angle) and prograde (0 deg heading angle) entry. The apoapsis altitude is computed using the trajectory state at atmospheric exit, defined at the same altitude as the entry interface (1000 km above the 1 bar pressure level). Atmospheric mean density uncertainties and random high frequency perturbations are used from Neptune-GRAM. Three sets of simulations were performed: 1) maximum range of Fminmax, 2) reduced atmospheric uncertainty, and 3) very low atmospheric uncertainty.

A. Maximum Range of Fminmax

The maximum atmospheric uncertainty case assumes that no improvement is available over data available from Neptune-GRAM and the aerocapture vehicle must accommodate the full range of Fminmax from -1 to +1.

Table 7 Monte Carlo uncertainties

Category	Variable	Nominal	$\pm 3\sigma$ or [min,max] or other	Distribution
Navigation	Entry flight-path angle (planet-relative)	-11.43 deg (retrograde) -13.85 deg (prograde)	± 0.33 deg ± 0.33 deg	Normal Normal
	Fminmax	-	[-1, +1]	Uniform
Atmosphere	Mean density uncertainty	0	3σ from Neptune-GRAM	Normal
	Random high frequency perturbation	-	rpscale = 1	Uniform
Aerodynamics	L/D	0.40	± 0.04	Uniform

Vehicle parameters used for the simulation are ballistic coefficient $\beta = 200 \text{ kg/m}^2$, drag coefficient $C_D = 1.59$, and nose radius $R_N = 1.0 \text{ m}$. The target apoapsis altitude is 400,000 km, and the apoapsis error tolerance used by the guidance algorithm is 10,000 km. The apoapsis prediction is initiated when the altitude rate exceeds -500 m/s and a guidance frequency of 2 Hz is used for the equilibrium glide phase. The onboard density estimation assumes perfect

knowledge of the total measured acceleration and other vehicle parameters and computes the density once during every guidance cycle. Guidance gain parameters used in the simulation are described in Appendix A. If the guidance algorithm predicts an apoapsis altitude lower than the target value, the equilibrium glide phase is terminated immediately and the vehicle flies full lift up. Higher guidance frequency can improve the apoapsis targeting, albeit at the cost of greater onboard computing requirements. Vehicle position and velocity states used by the guidance scheme will have uncertainties associated with inertial sensors but for the present study are assumed to be known perfectly. The maximum roll rate is constrained to 30 deg/s. Orbit inclination targeting during the aerocapture maneuver is not considered.

A high-fidelity 3-DoF simulation including gravity zonal harmonics up to J_4 , aerodynamic forces, Coriolis, and centrifugal forces is used to simulate the trajectory of a spacecraft flying in the vicinity of an oblate, rotating planet. The initial state for the entry simulation is the terminal state of the interplanetary approach trajectory using the B-plane targeting method [39]. The aerocapture trajectory is propagated from atmospheric entry to the atmospheric exit interface. The simulation uses an outer loop to propagate the actual vehicle trajectory, and an inner loop to simulate the guidance scheme. Five thousand aerocapture trajectories were simulated for both prograde and retrograde entry for different atmospheric uncertainty levels, and the results are used to assess guidance performance at Neptune using a blunt-body aeroshell.

1. Retrograde Entry

For the purpose of comparing the targeting accuracy for different cases evaluated, an arbitrary $\pm 50,000$ km bound about the target apoapsis is defined in this study. For the retrograde entry, all but one of the 5000 cases captured successfully with 75% of the cases achieving apoapsis within $\pm 50,000$ km of the target apoapsis (400,000 km). Figure 13 shows the histogram of the achieved apoapsis altitude. Figure 14 shows the dispersion in apoapsis and periapsis altitude. One trajectory failed to capture and is omitted from Figs. 13 and 14. The failure is attributed to low mean density (i.e. $F_{\min\max} = -1.0$), -0.4σ variation about the mean profile, and shallow EFPA = -11.02 deg ($+3.7\sigma$) along with the effect of high frequency perturbations.

Figure 15 shows the dispersion in peak deceleration and peak stagnation-point heat rate. The stagnation point heat rate is the sum of convective and radiative heating rates computed using engineering correlations [38]. The 99.87 percentile peak deceleration load is $14.32g$, an important parameter for aeroshell structural design and instrument qualification. The 99.87 percentile peak stagnation-point heat rate is $8,152$ W/cm 2 , an important parameter for TPS material selection and qualification. The heat rate is significantly higher compared to entry at Mars or Titan, but is expected to be within the performance envelope of the HEEET thermal protection system [35]. The 99.87 percentile propulsive ΔV requirement for the periapsis raise and the apoapsis correction maneuver are 315 m/s and 1,841 m/s respectively. The high apoapsis correction ΔV is due to a significant fraction of the cases undershooting the target apoapsis. The apoapsis undershoot in turn is attributed to selection of the target EFPA so as to minimize the risk of

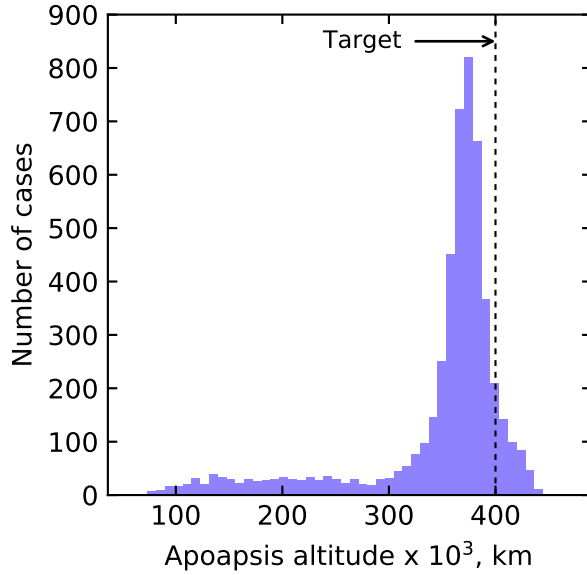


Fig. 13 Histogram of achieved apoapsis altitude for maximum range of Fminmax. Some cases resulted in significant undershoot (below 300,000 km).

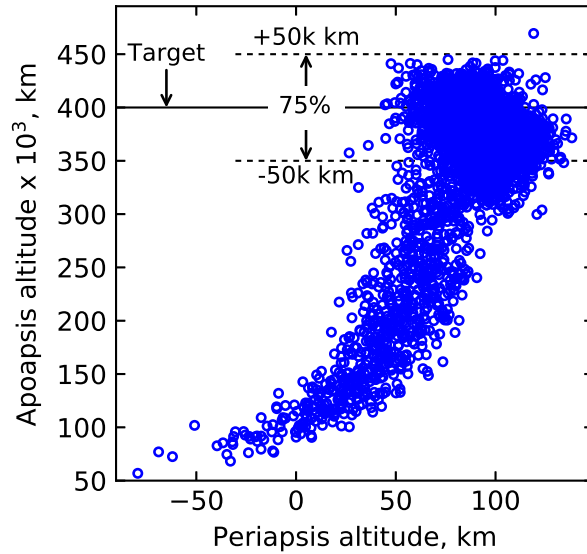


Fig. 14 Apoapsis dispersion for maximum range of Fminmax (retrograde). 75% of the cases achieved apoapsis within 50,000 km of the target.

escape in the event of minimum density atmosphere as described in Section VII. In the event of high density atmosphere, the nominal target EFPA results in apoapsis undershoot. The study emphasizes that the reported apoapsis correction ΔV values are strongly dependent on the 400,000 km target apoapsis. This is based on the study ground rule that Triton is a high priority science target for a future Neptune mission [29], and the orbit should be large enough to permit close Triton flybys. If a future mission chooses to forego this requirement to use a much smaller target apoapsis, the apoapsis

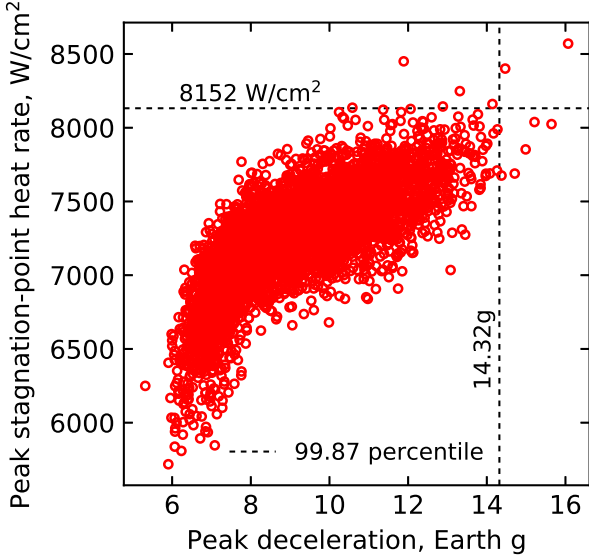


Fig. 15 Peak deceleration and peak stagnation-point heat rate for maximum range of Fminmax (retrograde).

correction ΔV values will be much smaller. The apoapsis correction ΔV values are also reported to compare the cost of correcting targeting errors for the different atmospheric uncertainty levels and vehicle L/D values considered in this study.

2. Prograde Entry

For the prograde entry, 98.48% of the cases captured successfully; 0.70% of the cases captured but with apoapsis altitudes greater than 500,000 km; 96% of the cases achieved apoapsis within $\pm 50,000$ km of the target apoapsis ($= 400,000$ km). Figure 16 shows the dispersion in apoapsis vs periapsis altitude. The trajectories which failed to capture and those which resulted in apoapsis altitude greater than 500,000 km are omitted from Fig. 16.

Figure 17 shows the dispersion in peak deceleration and peak stagnation-point heat rate. The 99.87 percentile peak deceleration load and stagnation-point heat rate is 13.40g and 1,675 W/cm² respectively. The 99.87 percentile stagnation-point heat rate for prograde entry is substantially lower than the retrograde entry case due to the lower planet-relative entry speed for prograde entry. The 99.87 percentile propulsive ΔV requirement for the periapsis raise maneuver and apoapsis correction maneuver is 180 m/s and 664 m/s respectively. Compared to the retrograde entry case where only 0.02% of the cases failed to capture, 1.5% of the cases failed to capture in the prograde case. Despite the lower capture probability, the fraction of cases which achieved apoapsis within $\pm 50,000$ km for the prograde case is 96% compared to 75% for the retrograde case. The cases which failed to capture or resulted in large orbits are attributed to combinations of shallow entry flight-path angles and low density atmosphere. Table 8 summarizes the percentiles for various parameters from Monte Carlo simulations with the full range of Fminmax.

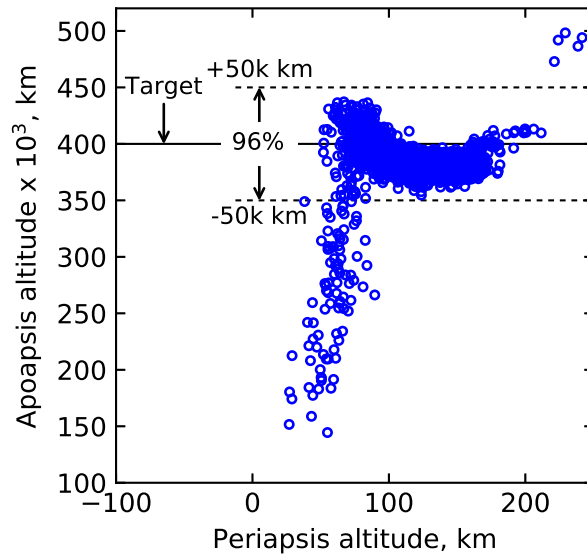


Fig. 16 Apoapsis vs periapsis altitude for maximum range of Fminmax (prograde). 96% of the cases achieved apoapsis altitude within 50,000 km of the target.

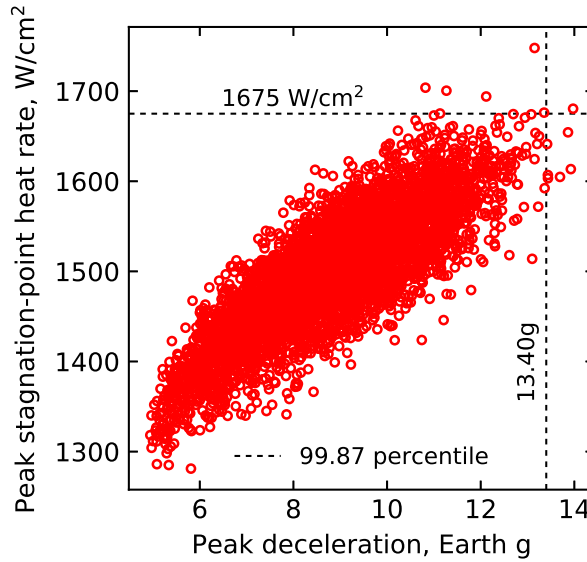


Fig. 17 Peak deceleration vs peak stagnation-point heat rate for maximum range of Fminmax (prograde). Note the reduction in heat rate compared to retrograde entry (Fig. 15).

B. Reduced Atmospheric Uncertainty

To investigate the effect of reduced atmospheric uncertainty from potential ground based observations and modelling efforts, the simulation is run with $-0.5 \leq F_{\text{minmax}} \leq +0.5$, and $rpscale = 0.5$. Other simulation parameters are the same as listed in Table 7. The results are reported for retrograde and prograde entry.

Table 8 Statistics from Monte Carlo simulation with full range of Fminmax

Retrograde entry					
Percentage captured	99.98%				
Percentage within $\pm 50,000$ km of target	74.94%				
Statistics for the 99.98% cases captured					
Parameter	Minimum	0.13 percentile	Median	99.87 percentile	Maximum
Apoapsis altitude, km	56,869	77,399	369,681	441,215	469,411
Peak deceleration, Earth g	5.32	6.00	9.01	14.32	16.07
Peak heat rate, W/cm ²	5,718	5,937	7,262	8,152	8,570
Periapsis raise ΔV , m/s	82.22	87.95	101.67	315.46	372.18
Apoapsis correction ΔV , m/s	0.04	0.18	51.43	1,840.71	2352.62
Total propulsive ΔV , m/s	94.83	95.22	152.84	2,158.23	2,724.80
Prograde entry					
Percentage captured	98.48%				
Percentage within $\pm 50,000$ km of target	95.88%				
Statistics for the 98.48% cases captured					
Parameter	Minimum	0.13 percentile	Median	99.87 percentile	Maximum
Apoapsis altitude, km	144,476	183,243	382,066	3,222,790	46,519,543
Peak deceleration, Earth g	4.75	4.95	8.87	13.40	13.97
Peak heat rate, W/cm ²	1,264	1,287	1,502	1,675	1,747
Periapsis raise ΔV , m/s	0.92	13.00	97.85	179.77	212.34
Apoapsis correction ΔV , m/s	0.08	0.33	29.88	680.80	942.22
Total propulsive ΔV , m/s	93.34	94.73	127.71	843.59	1154.76

1. Retrograde Entry

One hundred percent of the cases captured successfully. The percentage of cases that achieved apoapsis within $\pm 50,000$ km of the target is 93% as shown in Fig. 18 compared to 75% for the simulations with maximum atmospheric uncertainty. The improved apoapsis targeting lowers the 99.87 percentile apoapsis correction ΔV from 1,840 m/s (Table 8) to 328 m/s. Table 9 summarizes the Monte Carlo simulation results for the retrograde entry case.

2. Prograde Entry

99.98% of the cases captured successfully. 99.9% of the cases achieved apoapsis within $\pm 50,000$ km of the target apoapsis. Two cases (0.04%) captured but with apoapsis altitudes of 1 million km and 2.8 million km as compared to the target 400,000 km. Compared to the retrograde entry results shown in Fig. 18, the improved apoapsis targeting accuracy for the prograde entry lowered the 99.87 percentile apoapsis correction ΔV from 328 m/s to 55 m/s. Table 9 summarizes the results for the prograde entry case with reduced atmospheric uncertainty.

The reduced atmospheric uncertainty is likely more realistic compared to the conservative full range of Fminmax [48]. In addition, the present study uses a uniform distribution for range of Fminmax considered to provide conservative estimates. For future studies with more information were available to reduce the atmospheric uncertainties, a more reasonable choice would be a normal distribution about the most likely value of Fminmax.

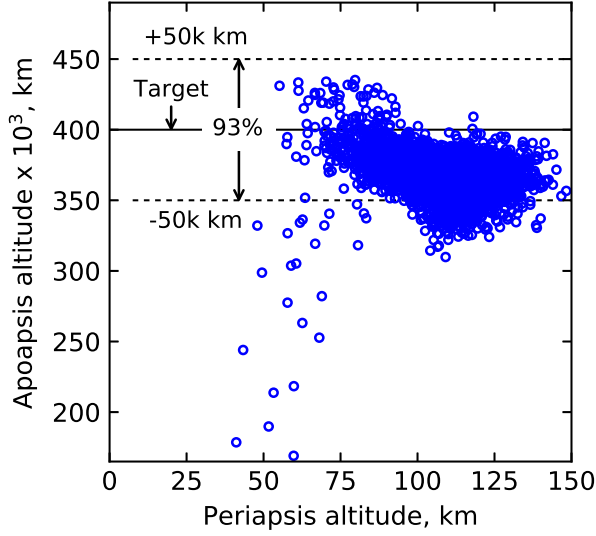


Fig. 18 Apoapsis vs periapsis altitude for reduced atmospheric uncertainty (retrograde entry). Note the improvement compared to the full range of Fminmax (Fig. 14)

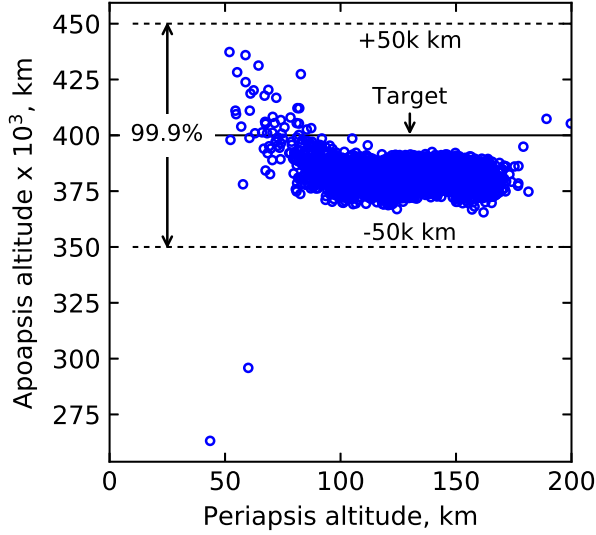


Fig. 19 Apoapsis vs periapsis altitude for reduced atmospheric uncertainty (prograde entry). 99.9% of the cases achieved apoapsis within 50,000 km of the target.

C. Very Low Atmospheric Uncertainty

To illustrate the effect of very low atmospheric uncertainty as may be possible using data from a pathfinder probe, the simulation is run with $0.6 \leq F_{\text{minmax}} \leq 0.8$, and $rpscale = 0.5$ as discussed in Sec. VII. Based on the discussion presented in Section VII the target EFPA is adjusted to -11.00 deg for the retrograde entry to allow for sufficient margin against escape and undershoot as indicated in Fig. 12. The target EFPA for the prograde entry is adjusted to -13.71 deg. Other simulation parameters are the same as listed in Section VIII.A. One hundred percent of the cases captured

Table 9 Statistics from Monte Carlo simulation with reduced atmospheric uncertainty

Retrograde entry					
Percentage captured	100%				
Percentage within $\pm 50,000$ km of target	92.60%				
Statistics for the 100% cases captured					
Parameter	Minimum	0.13 percentile	Median	99.87 percentile	Maximum
Apoapsis altitude, km	169,065	257,918	368,495	430,094	435,187
Peak deceleration, Earth g	4.94	5.92	7.52	11.82	12.26
Peak heat rate, W/cm ²	5,701	5,881	6,921	7,631	7,703
Periapsis raise ΔV , m/s	88.77	89.77	101.59	137.90	190.05
Apoapsis correction ΔV , m/s	0.14	1.16	53.33	328.47	754.09
Total propulsive ΔV , m/s	95.36	96.57	154.94	466.31	944.14
Prograde entry					
Percentage captured	99.98%				
Percentage within $\pm 50,000$ km of target	99.90%				
Statistics for the 99.98% cases captured					
Parameter	Minimum	0.13 percentile	Median	99.87 percentile	Maximum
Apoapsis altitude, km	263,169	368,826	381,941	425,621	2,778,000
Peak deceleration, Earth g	4.84	5.31	8.78	12.45	12.78
Peak heat rate, W/cm ²	1,280	1,317	1,489	1,645	1,681
Periapsis raise ΔV , m/s	14.97	90.93	97.85	101.46	136.46
Apoapsis correction ΔV , m/s	0.27	1.84	29.65	55.16	590.61
Total propulsive ΔV , m/s	95.65	97.35	127.43	155.79	605.58

successfully for both retrograde and prograde entry scenarios. Figures 20 and 21 show the achieved apoapsis vs periapsis altitude for retrograde and prograde entry respectively.

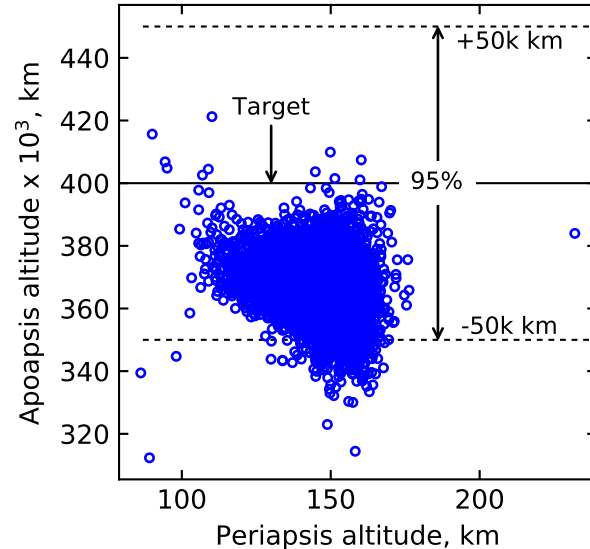


Fig. 20 Apoapsis vs periapsis altitude for very low atmospheric uncertainty (retrograde entry). Note the significant improvement compared to Figs. 14 and 18.

The results illustrate the effect of significant reduction of atmospheric uncertainties on apoapsis targeting accuracy.

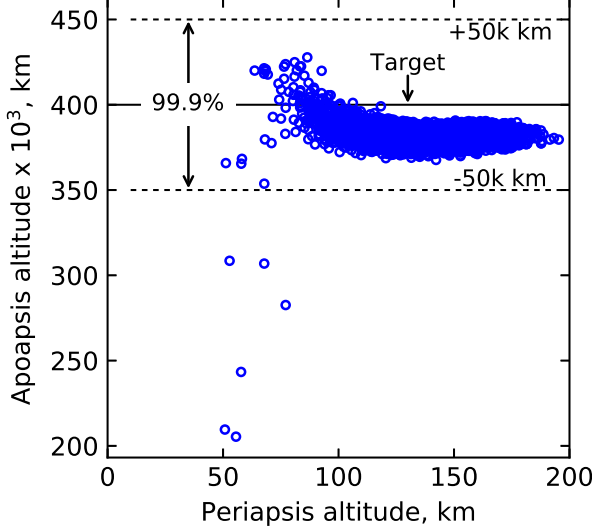


Fig. 21 Apoapsis vs periapsis altitude for very low atmospheric uncertainty (prograde entry). The accuracy is significantly improved compared to Fig. 16, but is similar to Fig. 19.

Apoapsis targeting is significantly improved compared to the simulations with the full range of $F_{\min\max}$ but show only a marginal improvement compared to $-0.5 \leq F_{\min\max} \leq +0.5$. The results indicate that if $-0.5 \leq F_{\min\max} \leq +0.5$ is considered acceptable atmospheric uncertainty, a pathfinder probe is not required to provide satisfactory apoapsis targeting. However, if available a pathfinder probe will provide additional safety margin against unknown atmospheric phenomena not accounted for in theoretical models. Table 10 summarizes the percentiles for various parameters for the very low atmospheric uncertainty scenario. For the retrograde entry, the 99.87 percentile total propulsive ΔV required is 233 m/s compared to 466 m/s for the simulations with $-0.5 \leq F_{\min\max} \leq +0.5$. In both Figs. 20 and 21, the mean apoapsis altitude falls slightly short of the target 400,000 km. This undershoot is attributed to two reasons: 1) The guidance algorithm predicts exit conditions with full lift up. Once the full lift command is initiated, the vehicle takes a few seconds to roll from its current orientation to full lift up but the delay is not accounted for in the guidance scheme. 2) The estimated density model is not perfect and occasionally shows significant deviation below the minimum altitude at which a measurement was available. Further fine tuning of the guidance parameters may reduce the targeting errors.

D. Sensitivity to Lift-to-Drag Ratio

The aerodynamic lift-to-drag L/D is the most important vehicle control parameter for trajectory analysis L/D [62], and the designer must account for the effect of variation in L/D on vehicle performance [63]. Even though the present study uses $L/D = 0.4$ as a nominal value for blunt-body aeroshells, the flight derived L/D values for the heritage Apollo entry vehicles range from 0.280 to 0.368 [62, 64]. For the purpose of the L/D sensitivity analysis, a capture probability of 98%, and 75% probability of achieving apoapsis within 50,000 km of the target are arbitrarily defined as the required

Table 10 Statistics from Monte Carlo simulation with very low atmospheric uncertainty

Retrograde entry					
Percentage captured	100%				
Percentage within $\pm 50,000$ km of target	95.08%				
Statistics for the 100% cases captured					
Parameter	Minimum	0.13 percentile	Median	99.87 percentile	Maximum
Apoapsis altitude, km	312,349	333,208	367,388	404,061	421,240
Peak deceleration, Earth g	3.91	5.49	6.68	9.86	10.83
Peak heat rate, W/cm ²	5,535	5,833	6,553	7,226	7,366
Periapsis raise ΔV , m/s	90.58	93.43	100.93	100.95	117.30
Apoapsis correction ΔV , m/s	1.65	4.39	55.35	123.59	171.63
Total propulsive ΔV , m/s	94.89	98.81	156.27	232.77	288.94
Prograde entry					
Percentage captured	100%				
Percentage within $\pm 50,000$ km of target	99.88%				
Statistics for the 100% cases captured					
Parameter	Minimum	0.13 percentile	Median	99.87 percentile	Maximum
Apoapsis altitude, km	205,390	359,571	381,427	421,065	427,788
Peak deceleration, Earth g	6.00	6.40	8.87	11.80	13.16
Peak heat rate, W/cm ²	1,317	1,337	1,468	1,586	1,597
Periapsis raise ΔV , m/s	89.95	91.36	97.79	105.09	164.91
Apoapsis correction ΔV , m/s	0.28	0.75	30.51	70.10	543.47
Total propulsive ΔV , m/s	95.32	95.88	128.38	175.15	708.38

criteria for mission success. A trade study is performed for $L/D = 0.35$ and 0.30 and various levels of atmospheric uncertainties to see if they offer sufficient control authority. The results are for retrograde entry.

For simulations with $-1 \leq F_{\min\max} \leq +1$, $L/D = 0.35$ and 0.30 did not meet the success criteria. To ensure capture for these cases, the target EFPA is substantially biased towards the steep end of the corridor. This results in satisfactory capture rates, but also results in a large number of cases undershooting the target apoapsis as seen in the apoapsis altitude statistics in Tables 11 and 12. The study recommends a vehicle with L/D of at least 0.40 for such large atmospheric uncertainties if the target apoapsis of $400,000$ km is desired. If the mission designer chooses to accept a wide apoapsis altitude distribution as listed in Tables 11 and 12, then $L/D = 0.35$ and 0.30 may be sufficient.

For $-0.5 \leq F_{\min\max} \leq +0.5$, $L/D = 0.35$ satisfied the success criteria, while $L/D = 0.30$ did not. For $L/D = 0.35$, only 83% achieved apoapsis within $50,000$ km of the target compared to 93% for $L/D = 0.40$. For $L/D = 0.30$, EFPA biasing is able to once again provide satisfactory capture rates, but a significant fraction of the cases undershoot the target apoapsis. L/D of at least 0.35 is recommended for atmospheric uncertainty of $-0.5 \leq F_{\min\max} \leq +0.5$.

For $+0.6 \leq F_{\min\max} \leq +0.8$, $L/D = 0.35$ offers sufficient control authority as seen in Table 11. One hundred percent of the cases captured, and the 99.87 percentile total propulsive ΔV required is 250 m/s. For $L/D = 0.30$, EFPA biasing is required to ensure vehicle capture, but 79% of the cases achieved apoapsis within $50k$ km of the target. The study recommends L/D of at least 0.30 for $+0.6 \leq F_{\min\max} \leq +0.8$. The results of the L/D trade study are summarized in Table 13 and the simulation statistics show the effect of L/D reduction in aerocapture performance.

Table 11 Statistics from Monte Carlo simulation with $L/D = 0.35$

$-1.0 \leq F_{\min\max} \leq +1.0$; Retrograde entry, EFPA = -11.58 deg (biased to the steep side to ensure capture)					
Percentage captured	100%				
Percentage within $\pm 50,000$ km of target	44.75%				
Statistics for the 100% cases captured					
Parameter	Minimum	0.13 percentile	Median	99.87 percentile	Maximum
Apoapsis altitude, km	26,799	28,526	293,630	441,328	448,812
Periapsis raise ΔV , m/s	86.67	87.96	124.00	489.27	503.09
Total propulsive ΔV , m/s	95.09	95.33	344.09	4,023	4,140
$-0.5 \leq F_{\min\max} \leq +0.5$; Retrograde entry, EFPA = -11.33 deg					
Percentage captured	100%				
Percentage within $\pm 50,000$ km of target	83.44%				
Statistics for the 100% cases captured					
Parameter	Minimum	0.13 percentile	Median	99.87 percentile	Maximum
Apoapsis altitude, km	73,049	92,774	368,664	436,622	442,759
Periapsis raise ΔV , m/s	87.30	88.30	101.50	282.54	325.74
Total propulsive ΔV , m/s	94.63	95.31	154.53	1,840	2,260
$+0.6 \leq F_{\min\max} \leq +0.8$; Retrograde entry, EFPA = -10.94 deg					
Percentage captured	100%				
Percentage within $\pm 50,000$ km of target	90.38%				
Statistics for the 100% cases captured					
Parameter	Minimum	0.13 percentile	Median	99.87 percentile	Maximum
Apoapsis altitude, km	287,017	326,223	364,423	407,931	430,583
Periapsis raise ΔV , m/s	88.54	92.26	101.39	111.37	125.62
Total propulsive ΔV , m/s	94.00	95.57	162.13	250.46	363.71

Table 12 Statistics from Monte Carlo simulation with $L/D = 0.30$

$-1.0 \leq F_{\min\max} \leq +1.0$; Retrograde entry, EFPA = -11.61 deg (biased to the steep side to ensure capture)					
Percentage captured	100%				
Percentage within $\pm 50,000$ km of target	20.00%				
Statistics for the 100% cases captured					
Parameter	Minimum	0.13 percentile	Median	99.87 percentile	Maximum
Apoapsis altitude, km	5,811	8,815	93,028	441,715	446,133
Periapsis raise ΔV , m/s	86.89	87.63	280.96	670.02	760.56
Total propulsive ΔV , m/s	95.54	95.87	1,835	5,781	6,225
$-0.5 \leq F_{\min\max} \leq +0.5$; Retrograde entry, EFPA = -11.33 deg (biased to the steep side to ensure capture)					
Percentage captured	100%				
Percentage within $\pm 50,000$ km of target	61.50%				
Statistics for the 100% cases captured					
Parameter	Minimum	0.13 percentile	Median	99.87 percentile	Maximum
Apoapsis altitude, km	54,508	55,198	361,561	426,603	430,035
Periapsis raise ΔV , m/s	89.25	89.42	103.04	367.21	370.15
Total propulsive ΔV , m/s	94.53	95.44	169.12	2,770	2,795
$+0.6 \leq F_{\min\max} \leq +0.8$; Retrograde entry, EFPA = -10.93 deg (biased to the steep side to ensure capture)					
Percentage captured	100%				
Percentage within $\pm 50,000$ km of target	79.44%				
Statistics for the 100% cases captured					
Parameter	Minimum	0.13 percentile	Median	99.87 percentile	Maximum
Apoapsis altitude, km	77,679	124,057	363,001	408,606	419,946
Periapsis raise ΔV , m/s	90.36	92.04	101.56	230.23	309.98
Total propulsive ΔV , m/s	93.82	95.07	164.97	1,370	2,145

Table 13 Percentage captured for various L/D and atmospheric uncertainty levels, values in parentheses indicate percentage of cases which achieved apoapsis within 50k km of the target.

Fminmax range	Remark	L/D		
		0.4	0.35	0.30
-1.0 to +1.0	Maximum	99.9% (75%)	100% ^a (45%)	100% ^a (20%)
-0.5 to +0.5	Reduced	100% (93%)	100% (83%)	100% ^a (62%)
0.6 to 0.8	Very low	100% (98%)	100% (90%)	100% ^a (79%)

^a With EFPA biasing to the steep side to ensure capture, resulting in apoapsis undershoot. See Tables 11 and 12 for apoapsis distribution.

IX. Summary

The present study investigated the feasibility and guidance performance of using heritage low- L/D blunt-body aeroshells for aerocapture at Neptune. Previous studies addressing Neptune aerocapture have used a mid- L/D vehicle which would in turn require the design, development, and testing of a new aeroshell before use in planetary missions. The lack of a mid- L/D vehicle motivated the investigation of techniques which may allow the use of low- L/D blunt-body aeroshells which have been extensively tested and flown. The aerocapture feasibility chart is used to concisely assess the coupling between interplanetary trajectory and vehicle performance trade space during preliminary mission design. Interplanetary trajectories with high arrival V_∞ allow the vehicle L/D requirement to be lowered while providing significantly shorter time of flight to Neptune. An Earth-Jupiter-Neptune trajectory launching in 2031 with a 7.87 year flight time is selected as the reference trajectory. Approach navigation analysis using state-of-the-art techniques have shown that delivery errors can be reduced compared to previous estimates. A new guidance algorithm with onboard density estimation is shown to be able to guide the spacecraft to the desired exit conditions even in worst case atmospheric uncertainties. The study concludes that the first hybrid aerocapture-propulsive approach does not allow the use low- L/D aeroshells for acceptable ΔV penalty, though this conclusion holds only for the 20-day science orbit considered. Smaller science orbits of the order of 1-day or smaller may use this approach without the prohibitively large ΔV associated with this approach. The second hybrid approach also does not allow the use of heritage blunt-body aeroshells. The study finds that a pathfinder probe is not necessary for aerocapture at Neptune if the risk of apoapsis undershoot is within acceptable limits. The pathfinder probe is recommended to be used as an option to enhance the safety margins and probability of mission success, but not as an enabling option for ice giant missions. Monte Carlo simulation is used to test guidance performance with combined navigation, atmospheric, and aerodynamic uncertainties.

X. Conclusion

Results indicate that the reduced navigation uncertainty and the improved guidance scheme enable a heritage blunt-body aeroshell with $L/D = 0.30\text{--}0.40$ to perform aerocapture at Neptune. The expected peak heat-rate is in the

range of 1600 to 8150 W/cm² and is within the capabilities of HEEET TPS material. For a vehicle with $L/D = 0.40$ entering retrograde and even with worst-case atmospheric uncertainty, 99.98% of the cases captured successfully and 75% of the cases achieved apoapsis altitude within 50,000 km of the target. For the lower atmospheric uncertainty levels considered, the L/D of 0.3–0.4 is shown to provide satisfactory performance. Additional study is required to estimate the TPS mass fraction of blunt-body vehicles entering Neptune at planet-relative speeds of 28–33 km/s.

Acknowledgments

The authors acknowledge Anastassios Petropoulos at the NASA Jet Propulsion Laboratory, and Nitin Arora formerly at the NASA Jet Propulsion Laboratory for providing the interplanetary trajectory data used in this study. The research described in this report was carried out at Purdue University and has been supported in part by the Jet Propulsion Laboratory, California Institute of Technology, under Contract Number 108436.

Appendix A: Guidance Parameters

The gain parameters used in the equilibrium glide phase guidance is computed based on the procedure developed by Cerimele and Gamble [55]. The vehicle altitude dynamic response can be shown to be:

$$\ddot{h} + \frac{C_L S}{m} G_h \dot{h} - \frac{C_L S}{m} G_{\bar{q}} (\bar{q} - \bar{q}_{\text{ref}}) = 0 \quad (5)$$

Equation 5 can be approximated as a linear second order system by assuming $\bar{q} = ah + b$, and the system response is characterized by

$$\omega_n^2 = -\frac{C_L S}{m} G_{\bar{q}} a \quad (6)$$

$$2\zeta\omega_n = \frac{C_L S}{m} G_h \quad (7)$$

For a vehicle with $m/C_L S = 500 \text{ kg/m}^2$, $L/D = 0.4$ entering Neptune atmosphere retrograde with planet-relative speed $V = 33.0 \text{ km/s}$, EFPA = -11.30 deg and using full lift up, the dynamic pressure as a function of altitude is shown in Fig. 22. A linear approximation can be made for the pressure profile as the vehicle descends below 300 km, and the aerodynamic forces become significant. Using $\omega_n = 0.05 \text{ rad/s}$ and $\zeta = 1.50$, the gain parameters can be calculated to be $G_h = 75.0$ and $G_{\bar{q}} = 7.41$. Hoewever, adjusting $G_{\bar{q}}$ to 3.0 was found to provide better performance and hence is the value used in the study. These values provided acceptable vehicle response, and were used for all simulations in the present study including the prograde cases for consistency. For a vehicle with different $m/C_L S$, or for different entry conditions, the above procedure can be used to recalculate the gain parameters.

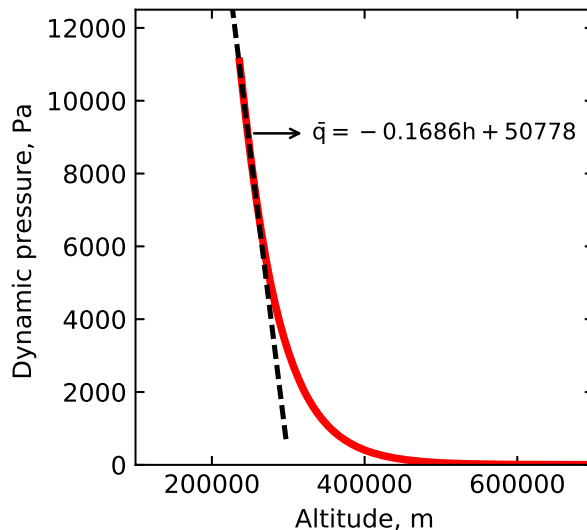


Fig. 22 Actual dynamic pressure profile (solid line) and linear approximation (dashed line) of the used to calculate guidance gain parameters. Based on the method developed by Cerimele and Gamble [55].

References

- [1] Lockwood, M. K., Edquist, K. T., Starr, B. R., Hollis, B. R., Hrinda, G. A., Bailey, R. W., Hall, J. L., Spilker, T. R., Noca, M. A., and O'Kongo, N., "Aerocapture Systems Analysis for a Neptune Mission," Tech. Rep. NASA/TM-2006-214300, NASA Langley Research Center, 2006. URL <https://ntrs.nasa.gov/archive/nasa/casi.ntrs.nasa.gov/20060012088.pdf>.
- [2] Spilker, T. R., "Significant Science at Titan and Neptune from Aerocaptured Missions," *Planetary and Space Science*, Vol. 53, No. 5, 2005, pp. 606–616. doi:10.1016/j.pss.2004.12.003.
- [3] Ingersoll, A. P., and Spilker, T. R., "A Neptune Orbiter with Probes Mission with Aerocapture Orbit Insertion," *Progress in Astronautics and Aeronautics: NASA Space Science Vision Missions*, Vol. 224, 2008, pp. 81–113. doi:10.2514/5.9781600866920.0081.0114.
- [4] Spilker, T. R., Adler, M., Arora, N., Beauchamp, P. M., Cutts, J. A., Munk, M. M., Powell, R. W., Braun, R. D., and Wercinski, P. F., "Qualitative Assessment of Aerocapture and Applications to Future Missions," *Journal of Spacecraft and Rockets*, Vol. 56, No. 2, 2018, pp. 536–545. doi:10.2514/1.A34056.
- [5] Carpenter, R., "Aeroassist Flight Experiment," Tech. Rep. ASE 396, Texas Space Grant Consortium, Austin, TX, 1992. URL <http://www.tsgc.utexas.edu/archive/PDF/AeroassistFlightExp.pdf>.
- [6] Wercinski, P., Henline, W., Tran, H., Milos, F., Papadopoulos, P., Chen, Y.-K., Venkatapathy, E., Tauber, M., Wercinski, P., Henline, W., et al., "Trajectory, Aerothermal Conditions, and Thermal Protection System Mass for the MARS 2001 Aerocapture Mission," *35th Aerospace Sciences Meeting and Exhibit*, 1997, p. 472. doi:10.2514/6.1997-472.
- [7] Powell, R., "Numerical Roll Reversal Predictor Corrector Aerocapture and Precision Landing Guidance Algorithms for the Mars Surveyor Program 2001 Missions," *23rd Atmospheric Flight Mechanics Conference*, AIAA, Boston, MA, 1998, p. 4574. doi:10.2514/6.1998-4574.
- [8] Cazaux, C., Naderi, F., Whetsel, C., Beaty, D., Gershman, B., Kornfeld, R., Mitcheltree, B., and Sackheim, B., "The NASA/CNES Mars Sample Return—A Status Report," *Acta Astronautica*, Vol. 54, No. 8, 2004, pp. 601–617. doi:10.1016/j.actaastro.2003.07.001.
- [9] Keys, A., Hall, J., Oh, D., and Munk, M., "Overview of a Proposed Flight Validation of Aerocapture System Technology for Planetary Missions," *42nd AIAA/ASME/SAE/ASEE Joint Propulsion Conference & Exhibit*, AIAA, Sacramento, CA, 2006, p. 4518. doi:10.2514/6.2006-4518.
- [10] Hall, J. L., Noca, M. A., and Bailey, R. W., "Cost-Benefit Analysis of the Aerocapture Mission Set," *Journal of Spacecraft and Rockets*, Vol. 42, No. 2, 2005, pp. 309–320. doi:10.2514/1.4118.
- [11] Lockwood, M. K., Starr, B. R., Paulson Jr, J. W., Kontinos, D. A., Chen, Y., Laub, B., Olejniczak, J., Wright, M. J., Takashima, N., and Justus, C. G., "Systems Analysis for a Venus Aerocapture Mission," Tech. Rep. NASA/TM-2006-214291, NASA Langley Research Center, Hampton, VA, 2006. URL <https://ntrs.nasa.gov/archive/nasa/casi.ntrs.nasa.gov/20060010899.pdf>.

- [12] Wright, H. S., Oh, D. Y., Westhelle, C. H., Fisher, J. L., Dyke, R. E., Edquist, K. T., Brown, J. L., Justh, H. L., and Munk, M. M., “Mars Aerocapture Systems Study,” Tech. Rep. NASA/TM-2006-214522, NASA Langley Research Center, Hampton, VA, 2006. URL <https://ntrs.nasa.gov/archive/nasa/casi.ntrs.nasa.gov/20060056070.pdf>.
- [13] Lockwood, M. K., Queen, E. M., Way, D. W., Powell, R. W., Edquist, K., Starr, B. W., Hollis, B. R., Zoby, E. V., Hrinda, G. A., and Bailey, R. W., “Aerocapture Systems Analysis for a Titan Mission,” Tech. Rep. NASA/TM-2006-214273, NASA Langley Research Center, Hampton, VA, 2006. URL <https://ntrs.nasa.gov/archive/nasa/casi.ntrs.nasa.gov/20060007561.pdf>.
- [14] Lu, Y., and Saikia, S. J., “Feasibility Assessment of Aerocapture for Future Titan Orbiter Missions,” *Journal of Spacecraft and Rockets*, Vol. 55, No. 5, 2018, pp. 1125–1135. doi:10.2514/1.A34121.
- [15] Lemmerman, L., and Wercinski, P., “Small Neptune Orbiter Using Aerocapture,” *AIP Conference Proceedings*, Vol. 387, AIP, 1997, pp. 101–110. doi:10.1063/1.51918.
- [16] Starr, B., Westhelle, C., and Masciarelli, J., “Aerocapture Performance Analysis for a Neptune-Triton Exploration Mission,” *AIAA Atmospheric Flight Mechanics Conference and Exhibit*, Providence, RI, 2004, p. 4955. doi:10.2514/6.2004-4955.
- [17] Masciarelli, J., Westhelle, C., and Graves, C., “Aerocapture Guidance Performance for the Neptune Orbiter,” *AIAA Atmospheric Flight Mechanics Conference and Exhibit*, Providence, RI, 2004, p. 4954. doi:10.2514/6.2004-4954.
- [18] Mazzaracchio, A., “Heat Shield Mass Minimization for an Aerocapture Mission to Neptune.” *International Journal of Aerospace Innovations*, Vol. 5, 2013. doi:10.1260/1757-2258.5.3-4.83.
- [19] Saikia, S. J., Petropoulos, A. E., and Cutts, J. A., “Aerocapture Assessment at Uranus and Neptune for NASA’s Ice Giant Studies,” Tech. Rep. PU-AAC-2016-MC-0002, Purdue University, West Lafayette, IN, 2016.
- [20] Florence, D. E., “Aerothermodynamic Design Feasibility of a Generic Planetary Aerocapture/aeromaneuver Vehicle,” *Thermophysics of Atmospheric Entry*, 1982, pp. 477–519. doi:10.2514/5.9781600865565.0477.0519.
- [21] Wercinski, P., Munk, M., Powell, R., Hall, J., Graves, C., and Partridge, H., “Aerocapture Technology Development Needs for Outer Planet Exploration,” Tech. Rep. NASA/TM-2002-211386, NASA Ames Research Center, Moffett Field, CA, 2002. URL <https://ntrs.nasa.gov/archive/nasa/casi.ntrs.nasa.gov/20020077966.pdf>.
- [22] Noca, M., and Bailey, R., “Mission Trades for Aerocapture at Neptune,” *40th AIAA/ASME/SAE/ASEE Joint Propulsion Conference and Exhibit*, AIAA, Fort Lauderdale, FL, 2004, p. 3843. doi:10.2514/6.2004-3843.
- [23] Laub, B., and Chen, Y., “TPS Challenges for Neptune Aerocapture,” *AIAA Atmospheric Flight Mechanics Conference and Exhibit*, AIAA, Providence, RI, 2006, p. 5178. doi:10.2514/6.2004-5178.
- [24] Dyke, R., and Hrinda, G., “Structural Design for a Neptune Aerocapture Mission,” *AIAA Atmospheric Flight Mechanics Conference and Exhibit*, AIAA, Providence, RI, 2004, p. 5179. doi:10.2514/6.2004-5179.
- [25] Starr, B., Westhelle, C., and Masciarelli, J., “Aerocapture Performance Analysis for a Neptune-Triton Exploration Mission,” *AIAA Atmospheric Flight Mechanics Conference and Exhibit*, AIAA, Providence, RI, 2004, p. 4955. doi:10.2514/6.2004-4955.

- [26] Bailey, R., Hall, J., Spilker, T., and O'Kongo, N., "Neptune Aerocapture Mission and Spacecraft Design Overview," *40th AIAA/ASME/SAE/ASEE Joint Propulsion Conference and Exhibit*, AIAA, Fort Lauderdale, FL, 2004, p. 3842. doi:10.2514/6.2004-3842.
- [27] Edquist, K. T., Prabhu, R. K., Hoffman, D. A., and Rea, J. R., "Configuration, Aerodynamics, and Stability Analysis for a Neptune Aerocapture Orbiter," *AIAA Atmospheric Flight Mechanics Conference and Exhibit*, AIAA, Providence, RI, 2004, p. 4953. doi:10.2514/6.2004-4953.
- [28] Hollis, B. R., Wright, M. J., Olejniczak, J., Takashima, N., Sutton, K., and Prabhu, D., "Preliminary Convective-Radiative Heating Environments for a Neptune Aerocapture Mission," *AIAA Atmospheric Flight Mechanics Conference and Exhibit*, AIAA, Providence, RI, 2004, p. 5177. doi:10.2514/6.2004-5177.
- [29] Hofstadter, M. D., Simon, A., Reh, K., and Elliot, J., "Ice Giants Pre-Decadal Study Final Report," Tech. Rep. JPL D-100520, NASA, Pasadena, CA, 2017. URL https://www.lpi.usra.edu/icegiants/mission_study/.
- [30] Moore, J., "Scientific Goals for Exploration of the Outer Solar System," Tech. Rep. OPAG-Report-Draft-Aug-2019, 2019. URL <https://www.lpi.usra.edu/opag/goals-08-28-19.pdf>.
- [31] Squyres, S. W., *Vision and Voyages for Planetary Science in the Decade 2013-2022*, National Academies Press, Washington D.C., 2011, Chap. 5.
- [32] Bayon, S., Falkner, P., and Pickering, A., "CDF Study Report: Ice Giants," Tech. Rep. CDF-187(C), ESA, Noordwijk, The Netherlands, 2019. URL <https://sci.esa.int/s/8JgpdVA>.
- [33] Agrawal, P., Allen, G. A., Sklyanskiy, E. B., Hwang, H. H., Huynh, L. C., McGuire, K., Marley, M. S., Garcia, J. A., Aliaga, J. F., and Moses, R. W., "Atmospheric entry studies for Uranus," *2014 IEEE Aerospace Conference*, IEEE, Big Sky, MT, 2014, pp. 1–19. doi:10.1109/AERO.2014.6836417.
- [34] Hughes, K. M., "Gravity-Assist Trajectories to Venus, Mars, and the Ice Giants: Mission Design with Human and Robotic Applications," Ph.D. Thesis, Purdue University, West Lafayette, IN, 2016.
- [35] Ellerby, D., Driver, D., Gasch, M., Mahzari, M., Milos, F., Owen, N., Peterson, K., Stackpoole, M., Venkatapathy, E., et al., "Overview of Heatshield for Extreme Entry Environment Technology (HEEET) Project," *16th International Planetary Probe Workshop (IPPW)*, Boulder, CO, June, 2018. URL https://www.colorado.edu/event/ippw2018/sites/default/files/attached-files/aeroentrytech_7_ellerby_presid594_pressslides_docid1160.pdf.
- [36] Milos, F. S., "Galileo Probe Heat Shield Ablation Experiment," *Journal of Spacecraft and Rockets*, Vol. 34, No. 6, 1997, pp. 705–713. doi:10.2514/2.3293.
- [37] Campagnola, S., Boutonnet, A., Martens, W., and Masters, A., "Mission Design for the Exploration of Neptune and Triton," *IEEE Aerospace and Electronic Systems Magazine*, Vol. 30, No. 7, 2015, pp. 6–17. doi:10.1109/MAES.2015.140119.

- [38] Bienstock, B., Atkinson, D., Atreya, S., Mahaffy, P., Baines, K., Wright, M., Wright, M., Stern, A., Steffes, P., Smith, D., Frampton, R., Peltz, L., Sichi, S., Masciarelli, J., Van Cleve, J., Murrow, D., and Landin, B., "NASA Vision Mission Neptune Orbiter with Probes," Tech. Rep. Contract No. NNH04CC41C, NASA, 2005.
- [39] Sergeyevsky, A. B., Snyder, G. C., and Cunniff, R. A., "Interplanetary Mission Design Handbook. Volume 1, part 2: Earth to Mars ballistic mission opportunities, 1990-2005," Tech. Rep. JPL-PUBL-82-43-VOL-1-PT-2, Pasadena, CA, 1983. URL <https://ntrs.nasa.gov/archive/nasa/casi.ntrs.nasa.gov/19840010158.pdf>.
- [40] D'Amario, L., and Watkins, M., "Mars Exploration Rovers - A New Standard for Interplanetary Navigation," *55th International Astronautical Congress*, Vancouver, Canada, 2004. doi:10.2514/6.IAC-04-Q.3.A.04.
- [41] Owen Jr., W. M., "Methods of Optical Navigation," *AAS Spaceflight Mechanics Conference*, New Orleans, LA, 2011. URL <https://trs.jpl.nasa.gov/handle/2014/41942>.
- [42] Evans, S., Taber, W., Drain, T., Smith, J., Wu, H.-C., Guevara, M., Sunseri, R., and Evans, J., "MONTE: The Next Generation of Mission Design and Navigation Software," *CEAS Space Journal*, Vol. 10, No. 1, 2018, pp. 79–86. doi:10.1007/s12567-017-0171-7.
- [43] Kizner, W., "A Method of Describing Miss Distances for Lunar and Interplanetary Trajectories," *Planetary and Space Science*, Vol. 7, 1961, pp. 125–131. doi:10.1016/0032-0633(61)90293-8.
- [44] Longuski, J. M., Todd, R. E., and Koenig, W. W., "Survey of Nongravitational Forces and Space Environmental Torques - Applied to the Galileo," *Journal of Guidance, Control, and Dynamics*, Vol. 15, No. 3, 1992, pp. 545–553. doi:10.2514/3.20874.
- [45] Stone, E., and Miner, E., "The Voyager 2 Encounter with the Neptunian System," *Science*, Vol. 246, No. 4936, 1989, pp. 1417–1421. doi:10.1126/science.246.4936.1417.
- [46] Justus, C., Duvall, A., and Keller, V., "Atmospheric Models for Aerocapture," *40th AIAA/ASME/SAE/ASEE Joint Propulsion Conference and Exhibit*, AIAA, Fort Lauderdale, FL, 2004. doi:10.2514/6.2004-3844.
- [47] Duvall, A., Justus, C., and Keller, V., "Global Reference Atmospheric Model (GRAM) Series for Aeroassist Applications," *43rd AIAA Aerospace Sciences Meeting and Exhibit*, AIAA, Reno, NV, 2005. doi:10.2514/6.2005-1239.
- [48] Justh, H., "Neptune-GRAM 2004 Documentation," Tech. Rep. Neptune-GRAM 2004, NASA Marshall Space Flight Center, Huntsville, AL, 2004.
- [49] Justus, C., Duvall, A., and Johnson, D., "Engineering-level Model Atmospheres for Titan and Neptune," *39th AIAA/ASME/SAE/ASEE Joint Propulsion Conference and Exhibit*, Huntsville, AL, 2003, p. 4803. doi:10.2514/6.2003-4803.
- [50] Dyakonov, A., Schoenenberger, M., and Van Norman, J., "Hypersonic and Supersonic Static Aerodynamics of Mars Science Laboratory Entry Vehicle," *43rd AIAA Thermophysics Conference*, New Orleans, LA, 2012, p. 2999. doi:10.2514/6.2012-2999.

- [51] Dutta, S., and Braun, R. D., “Statistical Entry, Descent, and Landing Performance Reconstruction of the Mars Science Laboratory,” *AIAA Atmospheric Flight Mechanics Conference*, National Harbor, MD, 2014, p. 0385. doi:10.2514/6.2014-0385.
- [52] Schoenenberger, M., Norman, J. V., Karlgaard, C., Kutty, P., and Way, D., “Assessment of the Reconstructed Aerodynamics of the Mars Science Laboratory Entry Vehicle,” *Journal of Spacecraft and Rockets*, Vol. 51, No. 4, 2014, pp. 1076–1093. doi:10.2514/1.A32794.
- [53] Hillje, E. R., “Entry Flight Aerodynamics from Apollo Mission AS-202,” Tech. Rep. NASA TN D-4185, Washington D. C., October, 1967. URL <https://ntrs.nasa.gov/archive/nasa/casi.ntrs.nasa.gov/19670027745.pdf>.
- [54] Way, D. W., Powell, R. W., Chen, A., Steltzner, A. D., San Martin, A. M., Burkhardt, P. D., et al., “Mars Science Laboratory: Entry, Descent, and Landing System Performance,” *Aerospace Conference, 2007 IEEE*, IEEE, Big Sky, MT, March 3–10, 2007, pp. 1–19. doi:10.1109/AERO.2007.352821.
- [55] Cerimele, C., and Gamble, J., “A Simplified Guidance Algorithm for Lifting Aeroassist Orbital Transfer Vehicles,” *23rd Aerospace Sciences Meeting*, Houston, TX, 1985, p. 348. doi:10.2514/6.1985-348.
- [56] Roelke, E., Hattis, P. D., and Braun, R., “Improved Atmospheric Estimation for Aerocapture Guidance,” *2019 AAS/AIAA Astrodynamics Specialist Conference*, Portland, ME, 2019.
- [57] Hamel, J. F., and Lafontaine, J. D., “Improvement to the Analytical Predictor-Corrector Guidance Algorithm Applied to Mars Aerocapture,” *Journal of Guidance, Control, and Dynamics*, Vol. 29, No. 4, 2006, pp. 1019–1022. doi:10.2514/1.20126.
- [58] Perot, E., and Rousseau, S., “Importance of an On-board Estimation of the Density Scale Geight for Various Aerocapture Guidance Algorithms,” *AIAA/AAS Astrodynamics Specialist Conference and Exhibit*, Monterey, CA, 2002, p. 4734. doi:10.2514/6.2002-4734.
- [59] Wagner, J., Wilhite, A., Stanley, D., and Powell, R., “An Adaptive Real Time Atmospheric Prediction Algorithm for Entry Vehicles,” *3rd AIAA Atmospheric Space Environments Conference*, Honolulu, HI, 2011, p. 3200. doi:10.2514/6.2011-3200.
- [60] Skalecki, L., Cerimele, C., and Gamble, J., “Meteorological Accuracy Requirements for Aerobraking Orbital Transfer Vehicles,” *22nd Aerospace Sciences Meeting*, Houston, TX, 1984, p. 30. doi:10.2514/6.1984-30.
- [61] Vinh, N. X., Busemann, A., and Culp, R. D., *Hypersonic and Planetary Entry Flight Mechanics.*, University of Michigan Press, Ann Arbor, MI, 1980, pp. 26–28.
- [62] Hillje, E. R., “Entry Aerodynamics at Lunar Return Conditions Obtained from the Flight of Apollo 4/AS-501,” Tech. Rep. NASA/TN D-5399, NASA Johnson Space Center, Houston, TX, 1969. URL <https://ntrs.nasa.gov/archive/nasa/casi.ntrs.nasa.gov/19690029435.pdf>.
- [63] Graves, C. A., and Harbold, J. C., “Apollo Experience Report: Mission Planning for Apollo Entry,” Tech. Rep. NASA/TN D-6725, NASA Johnson Space Center, Houston, TX, 1972. URL <https://ntrs.nasa.gov/archive/nasa/casi.ntrs.nasa.gov/19720013191.pdf>.

[64] Orloff, R., and Garber, S., *Apollo by the Numbers: A Statistical Reference*, NASA History Division, Washington, DC, 2000.